

# Efficient quadrature rules for finite element discretizations of nonlocal equations

Eugenio Aulisa<sup>\*</sup>   Giacomo Capodaglio<sup>†</sup>   Andrea Chierici<sup>‡</sup>   Marta D’Elia<sup>§</sup>

## Abstract

In this paper we design efficient quadrature rules for finite element discretizations of nonlocal diffusion problems with compactly supported kernel functions. Two of the main challenges in nonlocal modeling and simulations are the prohibitive computational cost and the nontrivial implementation of discretization schemes, especially in three-dimensional settings. In this work we circumvent both challenges by introducing a parametrized mollifying function that improves the regularity of the integrand, utilizing an adaptive integration technique, and exploiting parallelization. We first show that the “mollified” solution converges to the exact one as the mollifying parameter vanishes, then we illustrate the consistency and accuracy of the proposed method on several two- and three-dimensional test cases. Furthermore, we demonstrate the good scaling properties of the parallel implementation of the adaptive algorithm and we compare the proposed method with recently developed techniques for efficient finite element assembly.

## 1 Introduction

Nonlocal equations have become the model of choice in applications where the global behavior of the system is affected by long-range forces at small scales. In particular, these equations are preferable to partial differential equations (PDEs) in presence of anomalous behavior, such as superdiffusion and subdiffusion, multiscale behavior, and discontinuities or irregularities in the solution that cannot be captured by classical models. For these reasons, nonlocal models are currently employed in several scientific and engineering applications including surface or subsurface transport [7, 8, 24, 48, 49], fracture mechanics [31, 34, 51], turbulence [33, 42], image processing [9, 16, 28, 35] and stochastic processes [10, 18, 37, 39, 40].

The most general form [19] of a nonlocal operator for a scalar function  $u : \mathbb{R}^n \rightarrow \mathbb{R}$  is given by

$$\mathcal{L}u(\mathbf{x}) = 2 \int_{\mathbb{R}^n} (u(\mathbf{y}) - u(\mathbf{x}))\gamma(\mathbf{x}, \mathbf{y}) d\mathbf{y},$$

where  $\gamma$ , the kernel, is a compactly supported function over  $B_\delta(\mathbf{x})$ , the ball of radius  $\delta$  centered at  $\mathbf{x}$ . We refer to  $\delta$  as horizon or interaction radius; this quantity determines the extent of the nonlocal interactions and represents the length scale of the operator. The integral form allows one to catch long-range forces within the length scale and reduces the regularity requirements on the solutions. It also highlights the main difference between nonlocal models and PDEs, i.e., the fact that interactions can occur at distance, without contact. The kernel  $\gamma$  depends on the application and determines the regularity properties of the solutions; the choice of its parameters or functional form is among the most investigated open questions in the current nonlocal literature [42, 11, 20, 21, 30, 43, 44, 55, 57, 56]. In this work we limit ourselves to smooth integrable kernels since the treatment of more complex functions is not germane to the issues investigated in this paper, as clarified later on.

The integral nature of the operator poses several modeling and numerical challenges including the treatment of nonlocal interfaces [3, 12], the prescription of nonlocal boundary conditions [15, 23] and the design of efficient discretization schemes and numerical solvers [2, 13, 17, 22, 47, 50, 54]. In fact, the numerical solution of nonlocal equations becomes prohibitively expensive when the ratio between the interaction radius and the discretization size increases. Even though the nonlocal literature offers several examples of meshfree, particle-type discretizations [14, 45, 46, 50], in this paper we focus on finite element (FE) methods. This allows us to easily deal with nontrivial domains, achieve high-order accuracy, and use mesh adaptivity. Furthermore, the nonlocal vector calculus [26] provides a means for a rigorous stability

<sup>\*</sup>Department of Mathematics and Statistics, Texas Tech University, TX, USA.

<sup>†</sup>Computational Physics and Methods Group, Los Alamos National Laboratory, NM, USA

<sup>‡</sup>Department of Industrial Engineering, University of Bologna, Bologna, Italy

<sup>§</sup>Computational Science and Analysis, Sandia National Laboratories, CA, USA

and convergence analysis of variational methods as it allows us to analyze nonlocal diffusion problems in a similar way as elliptic PDEs [27].

When cast in a variational form, the nonlocal problem associated with the operator  $\mathcal{L}$  results in a bilinear form characterized by the following double integral

$$\int_{\Omega \cup \Gamma} \int_{(\Omega \cup \Gamma) \cap B_\delta(\mathbf{x})} (u(\mathbf{y}) - u(\mathbf{x}))(\varphi(\mathbf{y}) - \varphi(\mathbf{x}))\gamma(\mathbf{x}, \mathbf{y})d\mathbf{y}d\mathbf{x}$$

where we explicitly reported the domain of integration in the inner integral. Here,  $\Omega \in \mathbb{R}^n$  and  $\Gamma$  are the domain of interest and the corresponding “nonlocal boundary” and  $\varphi$  is an appropriate test function. Thus, the variational setting introduces further computational challenges. Not only do we have to numerically evaluate a double integral, but the integrand function is discontinuous, due to the compact support of  $\gamma$  and to the fact that, in FE settings, the tests functions are also compactly supported.

The paper by D’Elia et al.[22] thoroughly describes the challenges associated with nonlocal FE discretizations and proposes approximation techniques for efficient and accurate implementations. In particular, the authors introduce “approximate balls” that facilitate the assembly procedure by substituting the Euclidean ball  $B_\delta(\mathbf{x})$  with suitable polygonal approximations. They also suggest a set of quadrature rules for the outer and inner integration and analyze the convergence properties of the resulting scheme. With the same spirit, in this work, we propose an alternative way to efficiently evaluate the integral above by circumventing the issue of integrating a truncated function. The key idea of this paper is the introduction of a mollifier [41] to approximate the discontinuous kernel function; by doing so, the new, approximate, and parameterized kernel is a smooth function for which standard Gaussian quadrature rules can be employed over every element without compromising their accuracy. Additionally, we introduce adaptive quadrature rules for the numerical integration of the outer integral. In fact, contrary to intuition, sophisticated integration techniques for the outer integral are required in order to prevent the quadrature error from exceeding the FE one [22].

The main contributions of this paper are

- The introduction of a parametrized, smooth, approximate kernel, by means of a mollifier, that yields a smooth integrand over every element. This allows us to avoid the tedious and impractical task of determining the intersections of the ball with the elements, and hence represents a major advantage of our method in three-dimensional simulations.
- The design of adaptive quadrature rules for the outer integral and of a parallel algorithm for efficient simulations.
- The theoretical proof and numerical illustration of the convergence of the approximate, mollified solution to the analytic one as the mollified kernel approaches  $\gamma$ .
- The numerical illustration of the convergence of the mollified solution to the exact one as we refine the mesh and a numerical study of the dependence of the convergence behavior with respect to the parameters.
- The demonstration via two-dimensional and three-dimensional numerical tests of the scalability of our algorithm.

**Outline of the paper** In the following section we define the notation that is used throughout the paper and recall important results on nonlocal calculus. In Section 3 we introduce the mollifier function and the associated approximate, parametrized weak form of the nonlocal diffusion problem. We also analyze the convergence of the solution of the latter to the original weak solution. In Section 4 we describe the nonlocal FE discretization, with special focus on the assembly procedure, and briefly recall its challenges. In Section 5 we introduce adaptive quadrature rules for the numerical integration of the outer integral. In Section 6 we illustrate our theoretical results via two- and three-dimensional tests. We also discuss a parallel implementation of the FE assembly procedure and show the corresponding scaling results. Finally, we summarize our contributions in Section 7.

## 2 Preliminaries

Let  $\Omega \in \mathbb{R}^n$  be open and bounded,  $n = 1, 2, 3$ . Given some  $\delta > 0$ , we define the interaction domain  $\Gamma$  of  $\Omega$  as the set of all points not in  $\Omega$  that are within a  $\delta$  distance from points in  $\Omega$ , i.e.

$$\Gamma = \{\mathbf{y} \in \mathbb{R}^n \setminus \Omega : |\mathbf{x} - \mathbf{y}| \leq \delta \text{ for some } \mathbf{x} \in \Omega\}, \quad (1)$$

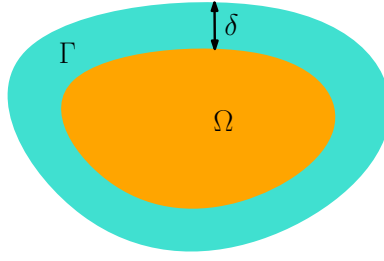


Figure 1: Example of domain  $\Omega$  with associated interaction domain  $\Gamma$ .

see Figure 1 for a graphical example in  $\mathbb{R}^2$ . Note that  $\Gamma$  depends on  $\delta$  even if it is not explicitly indicated. Let  $\gamma : \mathbb{R}^n \times \mathbb{R}^n \rightarrow \mathbb{R}$  be an integrable nonnegative symmetric kernel that is also radial<sup>a</sup>, namely  $\gamma(\mathbf{x}, \mathbf{y}) = \gamma(\mathbf{y}, \mathbf{x})$  and  $\gamma(\mathbf{x}, \mathbf{y}) = \gamma(|\mathbf{x} - \mathbf{y}|)$ . We also assume that  $\gamma$  has bounded support over the ball of radius  $\delta$  centered at  $\mathbf{x}$ , i.e.  $B_\delta(\mathbf{x})$ . For a scalar function  $u : \mathbb{R}^n \rightarrow \mathbb{R}$  we define the nonlocal Laplacian as

$$\mathcal{L}u(\mathbf{x}) = 2 \int_{\mathbb{R}^n} (u(\mathbf{y}) - u(\mathbf{x}))\gamma(\mathbf{x}, \mathbf{y}) d\mathbf{y}. \quad (2)$$

The strong form of a nonlocal Poisson problem is then given by: for  $f : \Omega \rightarrow \mathbb{R}$ , and  $g : \mathbb{R}^n \setminus \Omega \rightarrow \mathbb{R}$ , find  $u$  such that

$$\begin{cases} -\mathcal{L}u(\mathbf{x}) = f(\mathbf{x}), & \mathbf{x} \in \Omega \\ u(\mathbf{x}) = g(\mathbf{x}), & \mathbf{x} \in \Gamma \end{cases} \quad (3)$$

where the second condition in (3) is the nonlocal counterpart of a Dirichlet boundary condition for PDEs and it is referred to as *Dirichlet volume constraint*<sup>b</sup>. Such condition is required [27] to guarantee the well-posedness of (3). The weak form of the Poisson problem is obtained by multiplying the first equation in (3) by a test function  $\varphi = 0$  in  $\Gamma$  and by applying the nonlocal first Green's identity [26]. This yields

$$\begin{aligned} 0 &= \int_{\Omega} (-\mathcal{L}u - f) \varphi d\mathbf{x} \\ &= \iint_{(\Omega \cup \Gamma)^2} (u(\mathbf{y}) - u(\mathbf{x}))(\varphi(\mathbf{y}) - \varphi(\mathbf{x}))\gamma(\mathbf{x}, \mathbf{y}) d\mathbf{y} d\mathbf{x} - \int_{\Omega} f(\mathbf{x}) \varphi(\mathbf{x}) d\mathbf{x}, \end{aligned} \quad (4)$$

Then, the weak form of the nonlocal diffusion problem reads as follows. For  $f \in V'$  and  $g \in V_\Gamma$ , find  $u \in V$  such that

$$\mathcal{A}(u, v) = \mathcal{F}(v), \quad \forall v \in V_0, \quad \text{subject to } u = g \text{ in } \Gamma, \quad (5)$$

where

$$\begin{aligned} \mathcal{A}(u, \varphi) &= \iint_{(\Omega \cup \Gamma)^2} (u(\mathbf{y}) - u(\mathbf{x}))(\varphi(\mathbf{y}) - \varphi(\mathbf{x}))\gamma(\mathbf{x}, \mathbf{y}) d\mathbf{y} d\mathbf{x}, \\ \mathcal{F}(\varphi) &= \int_{\Omega} f(\mathbf{x}) \varphi(\mathbf{x}) d\mathbf{x}, \end{aligned} \quad (6)$$

and where the function spaces are defined as

$$\begin{aligned} V &= \{\varphi \in L^2(\Omega \cup \Gamma) : \|\varphi\| < \infty \text{ and } v|_{\mathbb{R}^n \setminus \Omega} = 0\} \\ V_0 &= \{\varphi \in V : \varphi|_{\Gamma} = 0\}, \\ V_\Gamma &= \{p : \Gamma \rightarrow \mathbb{R} : \exists \varphi \in V \text{ such that } \varphi|_{\Gamma} = p\}. \end{aligned} \quad (7)$$

Here, the *energy* semi-norm  $\|\cdot\|$  is defined as

$$\|\varphi\|^2 = \mathcal{A}(\varphi, \varphi), \quad (8)$$

the space  $V'$  is the dual space of  $V$  and  $V_\Gamma$  is a nonlocal trace space. Note that since the kernel is integrable and translation invariant, the energy semi-norm is a norm in the constrained space  $V_0$  and satisfies a Poincaré inequality [27]. Furthermore, by construction, the bilinear form  $\mathcal{A}(\cdot, \cdot)$  defines an inner product on  $V_0$  and it is continuous and coercive with respect to the energy norm  $\|\cdot\|$ . Finally, the latter is equivalent to the  $L^2$  norm; this allows us to establish an equivalence relationship between  $V$

<sup>a</sup>For a discussion on nonpositive kernels and nonsymmetric kernels, see [38] and [18], respectively.

<sup>b</sup>For definition and analysis of Neumann volume constraints we refer to [25] and for its numerical treatment we refer to, e.g., [23].

and  $L^2(\Omega \cup \Gamma)$ . Together with the continuity of  $\mathcal{F}$ , these facts yield the well-posedness of the weak form (5) [27].

As commonly done in the PDE context, we recast the problem in  $V_0$  by simply rewriting the solution as  $u = w + \tilde{g}$ , where  $w \in V_0$  and  $\tilde{g} \in V$  is an extension of  $g$  to zero into  $\Omega \cup \Gamma$ , known in the FE framework as a lifting function. Thus, equation (5) can be rewritten in terms of  $w$  as follows

$$\begin{aligned} \iint_{(\Omega \cup \Gamma)^2} (w(\mathbf{x}) - w(\mathbf{y})) (\varphi(\mathbf{x}) - \varphi(\mathbf{y})) \gamma(\mathbf{x}, \mathbf{y}) d\mathbf{y} d\mathbf{x} &= \int_{\Omega} f(\mathbf{x}) \varphi(\mathbf{x}) d\mathbf{x} \\ + \iint_{(\Omega \cup \Gamma)^2} (\tilde{g}(\mathbf{x}) - \tilde{g}(\mathbf{y})) (\varphi(\mathbf{x}) - \varphi(\mathbf{y})) \gamma(\mathbf{x}, \mathbf{y}) d\mathbf{y} d\mathbf{x}, &\quad \forall \varphi \in V_0, \end{aligned} \quad (9)$$

or, equivalently,

$$\mathcal{A}(w, \varphi) = \tilde{\mathcal{F}}(\varphi) \quad \forall \varphi \in V_0. \quad (10)$$

The latter is useful for implementation purposes as it allows us to automatically take into account the presence of a non-homogeneous Dirichlet volume constraint.

### 3 Weak form approximation

We introduce a parametrized approximation of the bilinear form  $\mathcal{A}$  defined in (6) with the purpose of obtaining a weak problem that is computationally less challenging. Specifically, the approximated bilinear form is associated with a parametrized kernel function that is still integrable, radial, and compactly supported, but not discontinuous in  $\Omega \cup \Gamma$ . This fact makes the numerical integration of the inner integral in, e.g., (5), a much simpler task, compared to the case of discontinuous kernel functions.

For simplicity of exposition, we rewrite the “exact” kernel  $\gamma$  as

$$\gamma(\mathbf{x}, \mathbf{y}) = C_{\delta} \eta(\mathbf{x}, \mathbf{y}) \mathcal{X}(\mathbf{y} \in B_{\delta}(\mathbf{x})) \quad (11)$$

where  $C_{\delta}$  is a scaling constant that guarantees that the nonlocal operator  $\mathcal{L}$  associated with  $\gamma$  is such that  $\mathcal{L} \rightarrow \Delta$  as  $\delta \rightarrow 0$ . Clearly, by definition,  $\eta(\mathbf{x}, \mathbf{y}) = \eta(|\mathbf{x} - \mathbf{y}|)$ . Given  $\varepsilon \in \mathbb{R}^+$ , we approximate the bilinear form  $\mathcal{A}(\cdot, \cdot)$  defined in (6) with the parametrized bilinear form  $\mathcal{A}_{\varepsilon}(\cdot, \cdot)$  obtained by replacing the kernel  $\gamma(\mathbf{x}, \mathbf{y})$  with

$$\gamma_{\varepsilon}(\mathbf{x}, \mathbf{y}) = C_{\delta, \varepsilon} \eta(\mathbf{x}, \mathbf{y}) \mu_{\delta, \varepsilon}(\mathbf{x}, \mathbf{y}), \quad (12)$$

where  $\mu_{\delta, \varepsilon}$  is an appropriately scaled mollifier function. Inspired by the mollifier function introduced in [41], for  $\varepsilon < \delta$  we define  $\mu_{\delta, \varepsilon} : \mathbb{R}^n \times \mathbb{R}^n \rightarrow \mathbb{R}$  as the following radial function

$$\mu_{\delta, \varepsilon}(|\mathbf{x} - \mathbf{y}|) = \begin{cases} 1 & \text{for } 0 \leq |\mathbf{x} - \mathbf{y}| < \delta - \varepsilon \\ \xi \left( \frac{(\delta - \varepsilon) - |\mathbf{x} - \mathbf{y}|}{\varepsilon} \right) & \text{for } \delta - \varepsilon \leq |\mathbf{x} - \mathbf{y}| \leq \delta + \varepsilon \\ 0 & \text{for } |\mathbf{x} - \mathbf{y}| > \delta + \varepsilon \end{cases} \quad (13)$$

$$\xi(r) = \left( \frac{128}{256} + \frac{315}{256}r - \frac{420}{256}r^3 + \frac{378}{256}r^5 - \frac{180}{256}r^7 + \frac{35}{256}r^9 \right),$$

where, for given  $\varepsilon > 0$ ,  $C_{\delta, \varepsilon}$  is such that the nonlocal operator  $\mathcal{L}_{\varepsilon}$ , associated with  $\gamma_{\varepsilon}$ , converges to  $\Delta$  as  $\delta \rightarrow 0$ . The constant  $C_{\delta, \varepsilon}$  is also such that it converges to  $C_{\delta}$  as  $\varepsilon \rightarrow 0$ . Furthermore, it follows from the definition of  $\mu_{\delta, \varepsilon}$  that

$$\lim_{\varepsilon \rightarrow 0} \mu_{\delta, \varepsilon}(\mathbf{x}, \mathbf{y}) = \mathcal{X}(\mathbf{y} \in B_{\delta}(\mathbf{x})),$$

which, together with the property of  $C_{\delta, \varepsilon}$ , implies that  $\gamma_{\varepsilon}$  converges pointwise to  $\gamma$  as  $\varepsilon \rightarrow 0$ . Note that the support of the mollifier is bigger than the one of the original kernel function  $\gamma$  as it corresponds to  $B_{\delta + \varepsilon}(\mathbf{x})$ . The parametrized bilinear form  $\mathcal{A}_{\varepsilon}(\cdot, \cdot)$  is therefore defined as follows

$$\mathcal{A}_{\varepsilon}(u, \varphi) = \iint_{(\Omega \cup \Gamma)^2} (u(\mathbf{y}) - u(\mathbf{x})) (\varphi(\mathbf{y}) - \varphi(\mathbf{x})) \gamma_{\varepsilon}(\mathbf{x}, \mathbf{y}) d\mathbf{y} d\mathbf{x}, \quad (14)$$

and consequently the approximate weak formulation of the nonlocal volume-constrained problem now reads: find  $u_{\varepsilon} \in V$  such that

$$\mathcal{A}_{\varepsilon}(u_{\varepsilon}, \varphi) = \mathcal{F}(\varphi) \quad \forall \varphi \in V_0 \quad \text{subject to } u_{\varepsilon} = g \text{ on } \Gamma. \quad (15)$$

Note that the weak formulation above is defined over the same function spaces of (5). This is allowed because the parametrized kernel  $\gamma_{\varepsilon}$  belongs to the same class of kernels as  $\gamma$ . As a consequence, problem (15) is also well-posed.

### 3.1 Convergence of the approximate weak solution

We find a bound for the energy norm of the difference between solutions of the weak form (5) and (15). First, we note that by subtracting (5) from (15) we obtain

$$\mathcal{A}(u, \varphi) = \mathcal{A}_\epsilon(u_\epsilon, \varphi) \quad \forall \varphi \in V_0. \quad (16)$$

Our ultimate goal is to find a bound for  $\|u - u_\epsilon\|$ , or, equivalently, for  $|\mathcal{A}(u - u_\epsilon, u - u_\epsilon)|$ , being  $u$  and  $u_\epsilon$  solutions of (5) and (15) respectively. We first consider a generic test function; equality (16) implies

$$\begin{aligned} |\mathcal{A}(u - u_\epsilon, \varphi)| &= |\mathcal{A}(u, \varphi) - \mathcal{A}(u_\epsilon, \varphi)| = |\mathcal{A}_\epsilon(u_\epsilon, \varphi) - \mathcal{A}(u_\epsilon, \varphi)| \\ &= \left| \iint_{(\Omega \cup \Gamma)^2} (u_\epsilon(\mathbf{x}) - u_\epsilon(\mathbf{y}))(\varphi(\mathbf{x}) - \varphi(\mathbf{y}))(\gamma_\epsilon(\mathbf{x}, \mathbf{y}) - \gamma(\mathbf{x}, \mathbf{y})) \, d\mathbf{y} \, d\mathbf{x} \right|. \end{aligned}$$

By expanding the product, we have

$$\begin{aligned} &\left| \iint_{(\Omega \cup \Gamma)^2} (u_\epsilon(\mathbf{x}) - u_\epsilon(\mathbf{y}))(\varphi(\mathbf{x}) - \varphi(\mathbf{y}))(\gamma_\epsilon(\mathbf{x}, \mathbf{y}) - \gamma(\mathbf{x}, \mathbf{y})) \, d\mathbf{y} \, d\mathbf{x} \right| \\ &\leq \iint_{(\Omega \cup \Gamma)^2} |u_\epsilon(\mathbf{x})\varphi(\mathbf{x})| |\gamma_\epsilon(\mathbf{x}, \mathbf{y}) - \gamma(\mathbf{x}, \mathbf{y})| \, d\mathbf{y} \, d\mathbf{x} \\ &\quad + \iint_{(\Omega \cup \Gamma)^2} |u_\epsilon(\mathbf{y})\varphi(\mathbf{y})| |\gamma_\epsilon(\mathbf{x}, \mathbf{y}) - \gamma(\mathbf{x}, \mathbf{y})| \, d\mathbf{y} \, d\mathbf{x} \\ &\quad + \iint_{(\Omega \cup \Gamma)^2} |u_\epsilon(\mathbf{x})\varphi(\mathbf{y})| |\gamma_\epsilon(\mathbf{x}, \mathbf{y}) - \gamma(\mathbf{x}, \mathbf{y})| \, d\mathbf{y} \, d\mathbf{x} \\ &\quad + \iint_{(\Omega \cup \Gamma)^2} |u_\epsilon(\mathbf{y})\varphi(\mathbf{x})| |\gamma_\epsilon(\mathbf{x}, \mathbf{y}) - \gamma(\mathbf{x}, \mathbf{y})| \, d\mathbf{y} \, d\mathbf{x}. \end{aligned}$$

By switching the order of integration and renaming dummy variables in the second and fourth terms above, we obtain

$$\begin{aligned} &2 \int_{\Omega \cup \Gamma} |u_\epsilon(\mathbf{x})\varphi(\mathbf{x})| \int_{\Omega \cup \Gamma} |\gamma_\epsilon(\mathbf{x}, \mathbf{y}) - \gamma(\mathbf{x}, \mathbf{y})| \, d\mathbf{y} \, d\mathbf{x} \\ &+ 2 \int_{\Omega \cup \Gamma} |\varphi(\mathbf{x})| \int_{\Omega \cup \Gamma} |u_\epsilon(\mathbf{y})| |\gamma_\epsilon(\mathbf{x}, \mathbf{y}) - \gamma(\mathbf{x}, \mathbf{y})| \, d\mathbf{y} \, d\mathbf{x} \\ &\leq 2c_1(\epsilon) \int_{\Omega \cup \Gamma} |u_\epsilon(\mathbf{x})\varphi(\mathbf{x})| \, d\mathbf{x} \\ &\quad + 2 \int_{\Omega \cup \Gamma} |\varphi(\mathbf{x})| \|u_\epsilon\|_{L^2(\Omega \cup \Gamma)} \|\gamma_\epsilon - \gamma\|_{L^2(\Omega \cup \Gamma)} \, d\mathbf{x} \\ &\leq 2c_1(\epsilon) \|u_\epsilon\|_{L^2(\Omega \cup \Gamma)} \|\varphi\|_{L^2(\Omega \cup \Gamma)} + 2c_2(\epsilon) |\Omega \cup \Gamma|^{\frac{1}{2}} \|u_\epsilon\|_{L^2(\Omega \cup \Gamma)} \|\varphi\|_{L^2(\Omega \cup \Gamma)}, \end{aligned} \quad (17)$$

where we used the Cauchy-Schwarz inequality for the outer and inner integral for the first and second term, respectively, and where

$$\begin{aligned} c_1(\epsilon) &= \max_{\mathbf{x} \in \Omega \cup \Gamma} \int_{B_{\delta+\epsilon}(\mathbf{x}) \cap (\Omega \cup \Gamma)} |\gamma_\epsilon(\mathbf{x}, \mathbf{y}) - \gamma(\mathbf{x}, \mathbf{y})| \, d\mathbf{y} \leq \int_{B_{\delta+\epsilon}(\mathbf{0})} |\gamma_\epsilon(\mathbf{0}, \mathbf{y}) - \gamma(\mathbf{0}, \mathbf{y})| \, d\mathbf{y}, \\ c_2^2(\epsilon) &= \max_{\mathbf{x} \in \Omega \cup \Gamma} \int_{B_{\delta+\epsilon}(\mathbf{x}) \cap (\Omega \cup \Gamma)} (\gamma_\epsilon(\mathbf{x}, \mathbf{y}) - \gamma(\mathbf{x}, \mathbf{y}))^2 \, d\mathbf{y} \leq \int_{B_{\delta+\epsilon}(\mathbf{0})} (\gamma_\epsilon(\mathbf{0}, \mathbf{y}) - \gamma(\mathbf{0}, \mathbf{y}))^2 \, d\mathbf{y}. \end{aligned}$$

We recall that, by definition,  $\gamma_\epsilon \rightarrow \gamma$  pointwise as  $\epsilon \rightarrow 0$ ; thus,  $c_i(\epsilon) \rightarrow 0$  as  $\epsilon \rightarrow 0$ , for  $i = 1, 2$ . Furthermore, thanks to the properties of  $\eta$  and  $\mu_{\delta, \epsilon}$ , the integrals above are well-defined.

To obtain the final estimate, we consider  $\varphi = u - u_\epsilon$  and recall that for the kernels considered in this work the energy norm  $\|\cdot\|$  is equivalent to the  $L^2$  norm. In particular there exists a positive constant

$C_{eq}$  such that  $\|\varphi\|_{L^2(\Omega \cup \Gamma)} \leq \|\varphi\|$ . Thus, we have the following estimate

$$\begin{aligned} \|u - u_\epsilon\|_{L^2(\Omega \cup \Gamma)}^2 &\leq C_{eq} \|u - u_\epsilon\|^2 \\ &= C_{eq} \mathcal{A}(u - u_\epsilon, u - u_\epsilon) \\ &\leq C_{eq} k(\epsilon) \|u_\epsilon\|_{L^2(\Omega \cup \Gamma)} \|u - u_\epsilon\|_{L^2(\Omega \cup \Gamma)}, \end{aligned}$$

where  $k(\epsilon)$  is obtained from the constants in (17). We finally conclude that

$$\|u - u_\epsilon\|_{L^2(\Omega \cup \Gamma)} \leq C_{eq} k(\epsilon) \|u_\epsilon\|_{L^2(\Omega \cup \Gamma)}, \quad (18)$$

where the constant  $k(\epsilon)$  is such that  $k(\epsilon) \rightarrow 0$  as  $\epsilon \rightarrow 0$ .

## 4 Finite element formulation

In this section we introduce a FE discretization of problem (10), highlight the associated computational challenges, and describe how the formulation introduced in the previous section helps circumventing them. Let  $\mathcal{T}_h$  be a shape-regular triangulation of  $\Omega \cup \Gamma$  into  $N_L$  finite elements  $\{\mathcal{E}_l\}_{l=1}^{N_L}$ ; the latter  $\mathcal{E}_l$  can either be triangles and/or quadrilaterals in two dimensions and tetrahedra and/or hexahedra in three dimensions<sup>c</sup>. The parameter  $h$  represents the size of the triangulation and corresponds to the larger element diameter. Also, let  $V_0^{N_h}$  be a finite dimensional subspace of  $V_0$  of dimension  $N_h$ , proportional to  $h^{-1}$ , and let  $\{\varphi_i\}_{i=1}^{N_h}$  be a basis for  $V_0^{N_h}$ . In this work we consider Lagrange basis functions over the triangulation  $\mathcal{T}_h$ . Thus, we can write the FE solution  $w_h$  of equation (10) as  $w_h(\mathbf{x}) = \sum_{i=1}^{N_h} W_i \varphi_i(\mathbf{x})$ . By using this expression and  $\varphi \in \{\varphi_i\}_{i=1}^{N_h}$ , equation (10) reduces to the algebraic system

$$A\mathbf{W} = \mathbf{F}, \quad (19)$$

where  $\mathbf{W} \in \mathbb{R}^{N_h}$  is the vector whose components are the degrees of freedom of the numerical solution  $w_h$ ,  $\mathbf{F}$  is such that  $\mathbf{F}_i = \tilde{\mathcal{F}}(\varphi_i)$ , and  $A$  is the stiffness matrix with entries

$$A_{ij} = \mathcal{A}(\varphi_i, \varphi_j) = \iint_{(\Omega \cup \Gamma)^2} (\varphi_i(\mathbf{x}) - \varphi_i(\mathbf{y})) (\varphi_j(\mathbf{x}) - \varphi_j(\mathbf{y})) \gamma(\mathbf{x}, \mathbf{y}) d\mathbf{y} d\mathbf{x}. \quad (20)$$

### 4.1 Circumventing computational challenges

The computation of the entries of the stiffness matrix  $A$  raises several diverse challenges. In this work we specifically focus on the challenges related to the presence of the indicator function in the definition of the kernel. Other challenges, such as the presence of singularities in fractional-type kernels or peridynamics kernels are not considered here. We point out that our method can be combined with any technique that takes into account the presence of the singularity. In fact, while the singularity is located at the center of the ball, the issues considered in this paper arise at the boundary. To make our description clear, we rewrite (20) by explicitly indicating the domain of integration, i.e.

$$\begin{aligned} A_{ij} &= C_\delta \int_{\Omega \cup \Gamma} \int_{(\Omega \cup \Gamma) \cap B_\delta(\mathbf{x})} (\varphi_i(\mathbf{x}) - \varphi_i(\mathbf{y})) (\varphi_j(\mathbf{x}) - \varphi_j(\mathbf{y})) \eta(\mathbf{x}, \mathbf{y}) d\mathbf{y} d\mathbf{x} \\ &= C_\delta \sum_{l=1}^{N_L} \sum_{k=1}^{N_L} \int_{\mathcal{E}_l} \int_{\mathcal{E}_k \cap B_\delta(\mathbf{x})} (\varphi_i(\mathbf{x}) - \varphi_i(\mathbf{y})) (\varphi_j(\mathbf{x}) - \varphi_j(\mathbf{y})) \eta(\mathbf{x}, \mathbf{y}) d\mathbf{y} d\mathbf{x}, \end{aligned} \quad (21)$$

where we split the integrals over the elements with the purpose of using composite quadrature rules. In fact, global quadrature rules used, e.g., over the ball  $B_\delta(\mathbf{x})$  for the inner integration are not convenient due to the basis functions' bounded support [22].

It is evident that the first challenge that one has to face is the integration over partial elements: when the element  $\mathcal{E}_k$  is not fully contained in the ball, standard quadrature rules such as Gauss quadrature rules defined over  $\mathcal{E}_k$  are not suitable due to the presence of the discontinuity induced by the indicator function. Thus, it is necessary to determine the intersection regions  $\mathcal{E}_k \cap B_\delta(\mathbf{x})$  and define quadrature rules there. This task, while affordable in two dimensions, becomes extremely complex and impractical in three dimensions. Furthermore, when  $B_\delta(\mathbf{x})$  is a Euclidean ball, such regions are curved so that appropriate approximations or quadrature rules for curved domains must be taken into account [22]. A

<sup>c</sup>See [22] for a description of appropriate triangulation techniques for nonlocal problems.

key observation is that these issues do not arise in case of smooth kernel functions, e.g. functions that do not abruptly jump to zero outside of  $B_\delta(\mathbf{x})$ , but that approach zero smoothly. This would allow the use of quadrature rules defined over the whole element  $\mathcal{E}_k$ , circumventing the issue of determining intersections or integrating over curved regions.

The parametrized kernel introduced in Section 3 is such that the transition to zero happens smoothly (as an example, for constant kernel functions  $\eta$ , the kernel function is a piece-wise polynomial in  $C^4$ ). Thus, the inner integration can be performed over the whole element  $\mathcal{E}_k$ , using accurate enough quadrature rules, without worrying about the presence of a discontinuity. We then propose to solve the approximate, parametrized problem

$$\mathcal{A}_\epsilon(w_{h,\epsilon}, \varphi_i) = \tilde{F}(\varphi_i), \quad \forall i = 1, \dots, N_h, \quad (22)$$

for which the entries of the stiffness matrix, that, with an abuse of notation, we still denote by  $A$ , read

$$A_{ij} = C_{\delta,\epsilon} \sum_{l=1}^{N_L} \sum_{k=1}^{N_L} \int_{\mathcal{E}_l} \int_{\mathcal{E}_k} (\varphi_i(\mathbf{x}) - \varphi_i(\mathbf{y})) (\varphi_j(\mathbf{x}) - \varphi_j(\mathbf{y})) \eta(\mathbf{x}, \mathbf{y}) \mu_{\delta,\epsilon}(\mathbf{x}, \mathbf{y}) d\mathbf{y} d\mathbf{x}. \quad (23)$$

By avoiding the problem of determining intersecting elements, this approach makes three-dimensional implementation a much simpler task.

**Remark 1** *The convergence of the solution  $w_{h,\epsilon}$  to the continuous solution  $w$  depends on both the discretization parameter  $h$  and the mollifying parameter  $\epsilon$ . An adaptive quadrature procedure, introduced in the following section, will further contribute to the overall approximation error, as we discuss and illustrate in Section 6.*

## 5 Adaptive quadrature rules

As already pointed out, the use of the mollifier, in place of the characteristic function, removes the difficulty of integrating discontinuous functions. The transition region of the mollifier has thickness  $2\epsilon$  and it is important to choose quadrature rules that can appropriately capture this region, especially if  $\epsilon \ll h$ . Note that the presence of the transition region affects the regularity of both the inner and the outer integrands. As we explain below, only one adaptive rule is necessary, applied to either the outer or inner integral. A quadrature rule with few points can be fast but is also inaccurate, one with many points can be accurate but is also expensive, especially in higher dimensions. To this end, adaptive quadrature rules have been proven to be accurate and efficient [41]. The advantage of using an adaptive scheme is that only the portion of the element overlapping with the transition region needs to be recursively refined, considerably reducing the computational time. Moreover, for fixed  $\epsilon$ , each partitioning has the effect of halving the ratio  $h/\epsilon$ . Thus, it is always possible to choose a number of adaptive refinements such that  $h \approx \epsilon$  and for which a quadrature rule with few points is accurate enough. Note that the adaptive quadrature rule devised here is not standard, because the refinement criterion is controlled by the distance between points in the outer and inner integrals. The details of the algorithm are given below.

We recall that we denote by  $A$  the stiffness matrix corresponding to the parametrized bilinear form  $\mathcal{A}_\epsilon$ . It is convenient to rewrite its entries as  $A_{ij} = A_{ij}^{11} + A_{ij}^{12} + A_{ij}^{21} + A_{ij}^{22}$ , where each term is given by

$$A_{ij}^{11} = \int_{\Omega \cup \Gamma} \int_{\Omega \cup \Gamma} \gamma_\epsilon(\mathbf{x}, \mathbf{y}) \varphi_i(\mathbf{x}) \varphi_j(\mathbf{x}) d\mathbf{y} d\mathbf{x}, \quad (24)$$

$$A_{ij}^{12} = - \int_{\Omega \cup \Gamma} \int_{\Omega \cup \Gamma} \gamma_\epsilon(\mathbf{x}, \mathbf{y}) \varphi_i(\mathbf{x}) \varphi_j(\mathbf{y}) d\mathbf{y} d\mathbf{x}, \quad (25)$$

$$A_{ij}^{21} = - \int_{\Omega \cup \Gamma} \int_{\Omega \cup \Gamma} \gamma_\epsilon(\mathbf{x}, \mathbf{y}) \varphi_i(\mathbf{y}) \varphi_j(\mathbf{x}) d\mathbf{y} d\mathbf{x}, \quad (26)$$

$$A_{ij}^{22} = \int_{\Omega \cup \Gamma} \int_{\Omega \cup \Gamma} \gamma_\epsilon(\mathbf{x}, \mathbf{y}) \varphi_i(\mathbf{y}) \varphi_j(\mathbf{y}) d\mathbf{y} d\mathbf{x}. \quad (27)$$

The following proposition allows us to express  $A_{ij}$  only as a sum of two of the terms above, as we show in Corollary 1.

**Proposition 1** *Let  $f_1$  and  $f_2 \in V$ , and let  $g(\mathbf{x}, \mathbf{y})$  be a symmetric function, then*

$$\int_{\Omega \cup \Gamma} \int_{\Omega \cup \Gamma} g(\mathbf{x}, \mathbf{y}) f_1(\mathbf{x}) f_2(\mathbf{y}) d\mathbf{y} d\mathbf{x} = \int_{\Omega \cup \Gamma} \int_{\Omega \cup \Gamma} g(\mathbf{x}, \mathbf{y}) f_1(\mathbf{y}) f_2(\mathbf{x}) d\mathbf{y} d\mathbf{x}. \quad (28)$$

**Proof 1**

$$\begin{aligned}
& \int_{\Omega \cup \Gamma} \int_{\Omega \cup \Gamma} g(\mathbf{x}, \mathbf{y}) f_1(\mathbf{x}) f_2(\mathbf{y}) d\mathbf{y} d\mathbf{x} \\
&= \int_{\Omega \cup \Gamma} \int_{\Omega \cup \Gamma} g(\mathbf{x}, \mathbf{y}) f_1(\mathbf{x}) f_2(\mathbf{y}) d\mathbf{x} d\mathbf{y} && \text{reversing the order} \\
&= \int_{\Omega \cup \Gamma} \int_{\Omega \cup \Gamma} g(\mathbf{x}, \mathbf{y}) f_1(\mathbf{y}) f_2(\mathbf{x}) d\mathbf{y} d\mathbf{x} && \begin{array}{l} \text{renaming variables} \\ \text{and using the symmetry of } g \end{array}
\end{aligned}$$

**Corollary 1** *The entries of the stiffness matrix  $A$  satisfy the following equality*

$$A_{ij} = 2A_{ij}^{11} + 2A_{ij}^{12} = 2A_{ij}^{21} + 2A_{ij}^{22}$$

**Proof 2** *The proof follows from the definition of  $A_{ij}$  and Proposition 1. Namely,  $A_{ij}^{11} = A_{ij}^{22}$  and  $A_{ij}^{12} = A_{ij}^{21}$ .*

Let  $Q_1 = \{(\mathbf{x}_{q_1}, w_{q_1})\}_{q_1}$  and  $Q_2 = \{(\mathbf{x}_{q_2}, w_{q_2})\}_{q_2}$  denote sets of quadrature points and associated weights representing two different *composite quadrature* rules for the numerical integration over the region  $\Omega \cup \Gamma$ . To preserve the equality between  $A_{ij}^{11}$  and  $A_{ij}^{22}$ , and between  $A_{ij}^{12}$  and  $A_{ij}^{21}$  we use  $Q_1$  and  $Q_2$  to numerically evaluate the inner and outer integrals as follows:

$$A_{ij}^{11} = \sum_{q_1 \in Q_1} \sum_{q_2 \in Q_2} \gamma_\epsilon(\mathbf{x}_{q_1}, \mathbf{x}_{q_2}) \varphi_i(\mathbf{x}_{q_1}) \varphi_j(\mathbf{x}_{q_1}) w_{q_2} w_{q_1}, \quad (29)$$

$$A_{ij}^{12} = \sum_{q_1 \in Q_1} \sum_{q_2 \in Q_2} \gamma_\epsilon(\mathbf{x}_{q_1}, \mathbf{x}_{q_2}) \varphi_i(\mathbf{x}_{q_1}) \varphi_j(\mathbf{x}_{q_2}) w_{q_2} w_{q_1}, \quad (30)$$

$$A_{ij}^{21} = \sum_{q_2 \in Q_2} \sum_{q_1 \in Q_1} \gamma_\epsilon(\mathbf{x}_{q_2}, \mathbf{x}_{q_1}) \varphi_i(\mathbf{x}_{q_1}) \varphi_j(\mathbf{x}_{q_2}) w_{q_1} w_{q_2}, \quad (31)$$

$$A_{ij}^{22} = \sum_{q_2 \in Q_2} \sum_{q_1 \in Q_1} \gamma_\epsilon(\mathbf{x}_{q_2}, \mathbf{x}_{q_1}) \varphi_i(\mathbf{x}_{q_1}) \varphi_j(\mathbf{x}_{q_1}) w_{q_1} w_{q_2}. \quad (32)$$

According to Corollary 1, only two terms among the ones above need to be computed. We choose to compute  $A_{ij}^{21}$  and  $A_{ij}^{22}$  in (31) and (32). We adopt an adaptive scheme for the outer quadrature and Gaussian composite quadrature rules for the inner integration over the elements that intersect the ball. These choices are empirical, i.e. they have been guided by numerical experiments that showed that for  $A_{ij}^{21}$  and  $A_{ij}^{22}$  using an adaptive quadrature for the outer integral is more efficient than using it for the inner one.

For every  $\mathcal{E}_l \in \mathcal{T}_h$  we define

$$\mathcal{K}_l = \{m \in \{1, \dots, N_L\} : \|\mathbf{x} - \mathbf{y}\|_{\ell_\infty} \geq \delta + \epsilon, \forall \mathbf{x} \in \mathcal{E}_l, \forall \mathbf{y} \in \mathcal{E}_m\}, \quad (33)$$

and  $\mathcal{J}_l = \mathcal{K}_l^c$ , i.e. the complement of  $\mathcal{K}_l$  in  $\{1, \dots, N_L\}$ . For  $k = 1, 2$  and  $l = 1, \dots, N_L$  let  $Q_k^l = \{(\mathbf{x}_{q_{k_l}}, w_{q_{k_l}})\}_{q_{k_l}} \subset Q_k$  denote the subset of  $Q_k$  composed of those quadrature points and weights obtained by only considering the quadrature points (and associated weights) that lie within element  $\mathcal{E}_l$ . Then, integrals (31) and (32) can be rewritten as

$$A_{ij}^{21} = \sum_{l=1}^{N_L} \sum_{q_{2_l} \in Q_2^l} \sum_{m \in \mathcal{J}_l} \sum_{q_{1_m} \in Q_1^m} \gamma_\epsilon(\mathbf{x}_{q_{2_l}}, \mathbf{x}_{q_{1_m}}) \varphi_i^m(\mathbf{x}_{q_{1_m}}) \varphi_j^l(\mathbf{x}_{q_{2_l}}) w_{q_{1_m}} w_{q_{2_l}}, \quad (34)$$

$$A_{ij}^{22} = \sum_{l=1}^{N_L} \sum_{q_{2_l} \in Q_2^l} \sum_{m \in \mathcal{J}_l} \sum_{q_{1_m} \in Q_1^m} \gamma_\epsilon(\mathbf{x}_{q_{2_l}}, \mathbf{x}_{q_{1_m}}) \varphi_i^m(\mathbf{x}_{q_{1_m}}) \varphi_j^l(\mathbf{x}_{q_{1_m}}) w_{q_{1_m}} w_{q_{2_l}}. \quad (35)$$

Note that in the equations above the terms in the sum are nonzero only when the support of the basis functions intersects the elements. An adaptive quadrature with midpoint refinement is adopted for  $Q_2^l$ . The pseudo-code that describes the adaptivity algorithm is reported in Algorithm 1: we employ recursive calls with input arguments  $L_{min}$ ,  $L_{max}$ ,  $L_{cur}$ ,  $\mathcal{E}_l$ , and  $\mathcal{J}_l$ . In each call  $L_{min}$  and  $L_{max}$  are fixed parameters, and represent the minimum and the maximum level of refinement, with  $L_{max} \geq L_{min} \geq 1$ .  $L_{cur}$  is the current level of refinement. In the initial call  $\mathcal{E}_l$  and  $\mathcal{J}_l$  are the ones defined above and  $L_{cur} = 1$ , while in the recursive calls these three arguments are subject to changes as described below.



- If  $L_{cur} < L_{min}$ , then  $\mathcal{E}_l$  is split in  $2^N$  sub-elements  $\mathcal{E}_{l_i}$  using the midpoint rule and for each of them the adaptive integration function is called again increasing  $L_{cur}$  by one and using the same index set  $\mathcal{J}_l$ .
- If  $L_{cur} = L_{max}$  integration is performed on  $\mathcal{E}_l$  for the outer integral and on each element indexed by  $\mathcal{J}_l$  for the inner integral, without any further refinement for  $\mathcal{E}_l$ . The numerical integration is performed using standard Gauss Legendre quadrature rules both for the outer and inner integrals.
- If  $L_{min} \leq L_{cur} < L_{max}$ , from the index set  $\mathcal{J}_l$  two new index sets  $\mathcal{J}_l^{int}$  and  $\mathcal{J}_l^{ref}$  are extracted, for which  $\mathcal{E}_l$  is either integrated or further refined. For any  $m$  in  $\mathcal{J}_l$ , the maximum distance from  $\mathcal{E}_m$  to  $\mathcal{E}_l$  is computed. If this distance is less than  $\delta - \varepsilon$ , then  $m$  is added to  $\mathcal{J}_l^{int}$ , otherwise the minimum distance from  $\mathcal{E}_m$  to  $\mathcal{E}_l$  is computed. If this distance is less than  $\delta + \varepsilon$  then  $m$  is added to the index set  $\mathcal{J}_l^{ref}$ . If  $\mathcal{J}_l^{int}$  is non-empty, integration is performed on  $\mathcal{E}_l$  for the outer integral and on each element indexed by  $\mathcal{J}_l^{int}$  for the inner integral. If  $\mathcal{J}_l^{ref}$  is non-empty, then  $\mathcal{E}_l$  is split in  $2^N$  sub-elements  $\mathcal{E}_{l_i}$  and for each of them the adaptive integration function is called again increasing  $L_{cur}$  by one and using  $\mathcal{J}_l^{ref}$  as index set.

**Algorithm 1** *function* ADAPTIVE INTEGRATION( $L_{min}$ ,  $L_{max}$ ,  $L_{cur}$ ,  $\mathcal{E}_l$ ,  $\mathcal{J}_l$ )

```

if  $L_{cur} < L_{min}$  then
  split  $\mathcal{E}_l$  into  $2^N$  new sub-elements  $\mathcal{E}_{l_i}$ 
  for  $i = 1, \dots, 2^N$  do
    ADAPTIVE INTEGRATION( $L_{min}$ ,  $L_{max}$ ,  $L_{cur} + 1$ ,  $\mathcal{E}_{l_i}$ ,  $\mathcal{J}_l$ )
  end for
else if  $L_{cur} = L_{max}$  then
  INTEGRATION( $\mathcal{E}_l$ ,  $\mathcal{J}_l$ )
else
   $\mathcal{J}_l^{int} = \emptyset$ 
   $\mathcal{J}_l^{ref} = \emptyset$ 
  for all  $m \in \mathcal{J}_l$  do
    if  $\max \text{dist}(\mathcal{E}_l, \mathcal{E}_m) < \delta - \varepsilon$  then
      add  $m$  to the index set  $\mathcal{J}_l^{int}$ 
    else if  $\min \text{dist}(\mathcal{E}_l, \mathcal{E}_m) < \delta + \varepsilon$  then
      add  $m$  to the index set  $\mathcal{J}_l^{ref}$ 
    end if
  end for
  if  $\mathcal{J}_l^{int} \neq \emptyset$  then
    INTEGRATION( $\mathcal{E}_l$ ,  $\mathcal{J}_l^{int}$ )
  end if
  if  $\mathcal{J}_l^{ref} \neq \emptyset$  then
    split  $\mathcal{E}_l$  into  $2^N$  new sub-elements  $\mathcal{E}_{l_i}$ 
    for  $i = 1, \dots, 2^N$  do
      ADAPTIVE INTEGRATION( $L_{min}$ ,  $L_{max}$ ,  $L_{cur} + 1$ ,  $\mathcal{E}_{l_i}$ ,  $\mathcal{J}_l^{ref}$ )
    end for
  end if
end if
end function

```

## 5.1 Approximate maximum and minimum distances between elements

Evaluating the exact distances between two elements can be computationally expensive, especially for unstructured three-dimensional meshes. Hence, in practice, we use conservative distances that are simple to compute in place of the maximum and the minimum. Namely, we first loop over the nodes of each element to find the minimum and maximum coordinates in each dimension, denote them by  $\mathbf{x}_{min}$ ,  $\mathbf{x}_{max}$  and by  $\mathbf{y}_{min}$ ,  $\mathbf{y}_{max}$ . Here  $\mathbf{x}_{min}$  and  $\mathbf{x}_{max}$  are the vectors containing the minimum and maximum coordinates of the bounding box containing  $\mathcal{E}_l$ . Similarly,  $\mathbf{y}_{min}$  and  $\mathbf{y}_{max}$  are the vectors containing the minimum and maximum coordinates of the bounding box containing  $\mathcal{E}_m$ . For each dimension  $k = 1, \dots, N$  evaluate the two quantities  $d_1^k = x_{min}^k - y_{max}^k$  and  $d_2^k = y_{min}^k - x_{max}^k$ . Finally, we approximate the maximum and

minimum distances with the two quantities

$$\text{aprx max dist}(\mathcal{E}_l, \mathcal{E}_m) = \sqrt{\sum_{k=1, \dots, N} \max(d_1^{k^2}, d_2^{k^2})}, \quad (36)$$

$$\text{aprx min dist}(\mathcal{E}_l, \mathcal{E}_m) = \max_{k=1, \dots, N} (\max(0, d_1^k, d_2^k)). \quad (37)$$

The approximate maximum distance in (36) is the maximum among the distances between opposite vertices of the two bounding boxes. For example in two dimensions it would be one among the distances  $\|SW - NE\|_{\ell_2}$ ,  $\|SE - NW\|_{\ell_2}$ ,  $\|NE - SW\|_{\ell_2}$  and  $\|NW - SE\|_{\ell_2}$ , with S meaning South, N meaning North and so on. This is true regardless of the reciprocal position of the two boxes. To better understand (37), consider the projections of the bounding boxes in the direction of  $k$ . Recall that, for fixed  $k$ , at least one between  $d_1^k$  and  $d_2^k$  is always negative. The other is positive only if the 2 projections do not overlap. In this case,  $\max(0, d_1^k, d_2^k)$  is the minimum (positive) distance between the 2 non-overlapping projections. Finally, we approximate the minimum distance with the largest projected distance.

It is easy to see that

$$\text{aprx max dist}(\mathcal{E}_l, \mathcal{E}_m) \geq \max \text{dist}(\mathcal{E}_l, \mathcal{E}_m), \quad (38)$$

$$\text{aprx min dist}(\mathcal{E}_l, \mathcal{E}_m) \leq \min \text{dist}(\mathcal{E}_l, \mathcal{E}_m), \quad (39)$$

where the sign of the inequalities assures the conservative approach in the adaptive integration algorithm. For a kernel whose support is identified by a ball in the topology defined by the  $L^2$  norm, the minimum distance could be also approximated by

$$\text{aprx min dist}(\mathcal{E}_l, \mathcal{E}_m) = \sqrt{\sum_{k=1, \dots, N} \max(0, d_1^k, d_2^k)^2}.$$

This last would give a sharper inequality in (39), however it would not work for the case where the support of the kernel is an  $L^\infty$  ball. In this work, for generality, we have chosen to always use formula (37). Note that (37) is also used in (33) in place of  $\|\cdot\|_{l_\infty}$  to identify the elements indexed by  $\mathcal{J}_l$ .

## 6 Numerical results

In this section, we present the results of numerical tests for FE discretizations of two-dimensional ( $n = 2$ ) and three-dimensional ( $n = 3$ ) problems. These results allow us to illustrate the theoretical results presented in the previous sections and highlight the efficiency of our approach.

We first show the consistency of the proposed method; specifically, fixing the mesh and letting the maximum level of adaptive refinement  $L_{max}$  increase, we study the behavior of the discretization error with respect to an analytic solution that belongs to the FE space. Then, we investigate the convergence of discretized solutions to the continuous one as the mesh is refined. To better understand the behavior of the algorithm and the specific sources of error, we devised a specific numerical test to isolate the error induced by the presence of the mollifier and analyze the convergence behavior with respect to  $\varepsilon$ . Accuracy comparisons with the algorithm proposed in the paper by D'Elia et al. [22] are also provided.

Due to the intrinsically high computational costs of nonlocal simulations, a parallel implementation of the algorithm is proposed and its scalability properties are analyzed both in two and three dimensions.

The two-dimensional tests are carried out on quadrilateral, triangular, and mixed meshes, i.e. meshes consisting of both quadrilateral and triangular elements. The three-dimensional simulations are carried out on a hexahedral mesh.

We consider constant kernels supported on Euclidean balls of radius  $\delta$ . To guarantee the consistency of the nonlocal diffusion operator with the classical Laplacian for polynomials up to degree three and its convergence to the classical Laplacian as  $\delta \rightarrow 0$ , we select the constants  $C_\delta$  and  $C_{\delta, \varepsilon}$  in (11) and (12), respectively, as follows

$$\begin{aligned} n = 2 : \quad C_\delta &= \frac{4\kappa}{\pi\delta^4}, & C_{\delta, \varepsilon} &= \frac{C_\delta}{1 + \frac{6}{11} \left(\frac{\varepsilon}{\delta}\right)^2 + \frac{3}{143} \left(\frac{\varepsilon}{\delta}\right)^4}, \\ n = 3 : \quad C_\delta &= \frac{15\kappa}{4\pi\delta^5}, & C_{\delta, \varepsilon} &= \frac{C_\delta}{1 + \frac{10}{11} \left(\frac{\varepsilon}{\delta}\right)^2 + \frac{15}{143} \left(\frac{\varepsilon}{\delta}\right)^4}. \end{aligned}$$

For sufficiently smooth  $u$ , these choices guarantee quadratic convergence of the nonlocal Laplacian to the local one for  $\delta \rightarrow 0$ :

$$\mathcal{L}u(\mathbf{x}) = \Delta u(\mathbf{x}) + O(\delta^2) \quad \text{and} \quad \mathcal{L}_\varepsilon u(\mathbf{x}) = \Delta u(\mathbf{x}) + O(\delta^2).$$

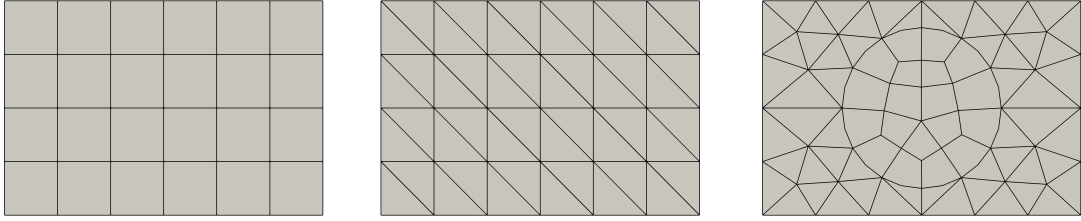


Figure 2: Meshes used for the two-dimensional numerical simulations: quadrilateral (left, number of degrees of freedom with linear FE discretization  $N_h = 35$ , and  $N_h = 93$  for quadratic FE discretization), triangular (center,  $N_h = 35$  for linear FE,  $N_h = 117$  for quadratic FE) and mixed (right,  $N_h = 58$  for linear FE,  $N_h = 190$  for quadratic FE).

**Sources of numerical error** Let  $u_h$  be the FE solution; the numerical error can heuristically be split into three separate contributions, i.e.

$$\|u - u_h\|_{L^2(\Omega \cup \Gamma)} \leq C_1 h^{p_1} + C_2 \varepsilon^{p_2} + E_i(\varepsilon, h, L_{max}), \quad (40)$$

where,  $h$  is the characteristic size of the mesh,  $C_1$  and  $C_2$  are positive constants independent of  $h$ ,  $\varepsilon$  and  $L_{max}$ , and  $p_1$  and  $p_2$  are positive integers that represent the rates of convergence with respect to  $h$  and  $\varepsilon$ , respectively. The first term on the right-hand side is the interpolation error and depends on the FE family used to discretize the problem<sup>d</sup>. The second term is the error induced by the presence of the mollifier and, in the  $L^2$  metric, it is bounded by the expression in (18). The last term,  $E_i$ , is the numerical integration error, that for fixed external and internal Gauss quadrature rules depends on  $\varepsilon$ ,  $h$  and  $L_{max}$ .

For  $h \rightarrow 0$  or  $L_{max} \rightarrow \infty$  the integration error  $E_i$  vanishes, whereas for  $\varepsilon \rightarrow 0$  it increases, since the transition to zero of the mollifier features higher gradients. In all simulations we empirically set the integration parameters so that the integration error  $E_i$  could be negligible compared to  $C_1 h^{p_1} + C_2 \varepsilon^{p_2}$ . In such a context,  $\varepsilon$  cannot be selected independently of  $h$  or  $L_{max}$ ; explicit dependence is provided in each simulation.

## 6.1 Two-dimensional tests

Two-dimensional numerical simulations of nonlocal operators can be found in several works in literature, see, e.g., [36], [53], and [52]. However, such studies are often designed for structured mesh only. On the other hand, our method can be applied to any type of mesh. We consider the domain  $\Omega = [-0.6, 0.6] \times [-0.4, 0.4]$  and three different meshes, see Figure 2 for a coarse example. Linear and quadratic Lagrange FE spaces are considered. Unless otherwise stated, we use Gauss-Legendre  $3 \times 3$  product rule for quadrilateral elements and Dunavant 7-point rule for triangles. In all tests we consider the error with respect to an analytic, manufactured solution,  $u(\mathbf{x})$ . For all  $\mathbf{x} \in \Gamma$ , the nonlocal Dirichlet volume constraint is set to  $g(\mathbf{x}) = u(\mathbf{x})$  and the forcing term is known analytically as  $f(\mathbf{x}) = -\mathcal{L}u(\mathbf{x})$ .

**Consistency** We choose  $u \in V^{N_h}$ , so that the interpolation error contribution in (40) is identically zero, regardless of  $h$ . We compute the discretization error  $\|u - u_h\|_{L^2}$  for a fixed mesh while increasing the values of the maximum level of adaptivity  $L_{max}$ .

For the linear manufactured solution  $u = 1 + x + y$  the forcing term is  $f(\mathbf{x}) = 0$ . In this case the numerical errors are always zero for both the linear and the quadratic FE spaces, for any  $L_{max}$  and  $\varepsilon$ . Although welcome, this result is an over-achievement, as it is obtained only because the forcing terms are zero. Thus, it should not be taken as a reference. For the quadratic manufactured solution  $u = x^2 + y^2$  the forcing term is  $f(\mathbf{x}) = -2$ . In this case we consider only the quadratic FE space, because it is the only one that can reproduce exactly the solution. We choose  $\varepsilon$  as

$$\varepsilon = \varepsilon_0 \left(\frac{3}{4}\right)^{L_{max}-3}$$

so that  $\varepsilon \rightarrow 0$  for  $L_{max} \rightarrow \infty$ , i.e. for  $L_{max} \rightarrow \infty$  both the mollifier and the integration errors in (40) vanish.

In Table 1 we report the errors of the numerical tests for the quadrilateral (QUAD) and triangular (TRI) meshes after one refinement, together with all the values of the parameters  $h$ ,  $\delta$ ,  $\varepsilon_0$  and  $L_{min}$ .

<sup>d</sup>For convergence rates of FE discretizations in presence of integrable kernels, we refer the reader to [27].

Table 1: Consistency test: errors  $\|u - u_h\|_{L^2}$  as  $L_{max}$  increases for  $u = x^2 + y^2$ ,  $h = 0.1$ ,  $\delta = 0.2$ ,  $\varepsilon_0 = 0.0125$ ,  $L_{min} = 1$ ,  $\varepsilon = \varepsilon_0(3/4)^{L_{max}-3}$  and quadratic FE.

$L_{max}$	QUAD	TRI
3	8.123E-05	2.713E-05
4	1.278E-05	2.052E-06
5	3.453E-07	1.193E-07
6	1.793E-09	1.774E-09
7	7.073E-10	5.479E-11

The  $L^2$ -norm of the error decreases down to machine precision, when  $L_{max}$  is increased, for both quadrilateral and triangular meshes, illustrating the consistency of the implemented adaptivity method in two dimensions.

**$h$ -Convergence** We consider the convergence with the respect to the grid size  $h$  on quadrilateral, triangular and mixed meshes. We use the manufactured solution  $u(\mathbf{x}) = x^3 + y^3$  for which the corresponding source term is given by  $f(\mathbf{x}) = -\mathcal{L}u(\mathbf{x}) = -\Delta u(\mathbf{x}) = -6(x + y)$  for  $\mathbf{x} \in \Omega$ . We analyze the convergence of the finite FE adaptive nonlocal solution  $u_h$  to the analytic solution  $u$  as we progressively halve the mesh size  $h$  by operating on a parameter referred to as  $ml$ , as shown in (41). We consider fixed  $L_{max}$ ,  $L_{min}$ , and  $\delta$ , whereas  $h$  and  $\varepsilon$  depend on  $ml$  (mesh level) as follows

$$h = h_0 \left(\frac{1}{2}\right)^{ml-2} \quad \text{and} \quad \varepsilon = \varepsilon_0 \left(\frac{2}{3}\right)^{ml-2}. \quad (41)$$

In Table 2 we report the values of  $\|u - u_h\|_{L^2}$  and the corresponding rate of convergence  $p$  as  $ml$  grows, evaluated in full awareness with respect to  $h$  only, with the approximate formula

$$p \cong \ln(E(h)/E(h/2)) / \ln(2). \quad (42)$$

For linear FE discretization we obtain quadratic convergence. This is optimal since it resembles the optimal convergence rate  $p_1 = 2$  of the interpolation error [27]. Namely, it indicates that in (40) the mollifier and the integration errors are negligible with respect to the interpolation error. Instead, in case of quadratic FE discretization, the observed rate is  $p \approx 3$  (similar to the optimal one  $p_1 = 3$ ) only for  $ml \leq 4$ , but it deteriorates for higher values of  $ml$ , i.e. as we refine the meshes (this behavior happens consistently on all the tested meshes, quadrilateral, triangular and mixed). This is due to the combined effect of the mollifier and integration errors that start dominating for  $h \rightarrow 0$ . Since  $\varepsilon \propto (2/3)^{ml-2}$ , the mollifying function defined in (13) exhibits a sharper gradient as we increase  $ml$  inducing a less accurate numerical integration, and, hence, higher values of  $E_i$ . Moreover, since the mesh refinement significantly reduces the interpolation error  $C_1 h^{p_1}$ , as we increase  $ml$  the error contribution  $C_2 \varepsilon^{p_2}$  becomes dominant affecting the overall convergence rate  $p$ .

We further test the convergence rate with respect to  $h$  considering the fourth-degree polynomial

$$u(\mathbf{x}) = x^4 + y^4, \quad (43)$$

for which the corresponding source term is given by  $f(\mathbf{x}) = -12(x^2 + y^2) - \delta^2$  for  $\mathbf{x} \in \Omega$ . Similarly to the previous test, in Table 3 we report the numerical results for linear and quadratic FE discretizations, on quadrilateral, triangular and mixed meshes. Again,  $p \approx 2$  for all the linear discretizations, while  $p \approx 3$  for quadratic discretizations only for  $ml \leq 3$ . Same considerations as for the previous test can be inferred.

**$\varepsilon$ -Convergence** We analyze the contribution of the mollifier to the discretization error, i.e.  $C_2 \varepsilon^{p_2}$  in (40). We consider the fourth-order polynomial in (43) on a triangular mesh with a quadratic FE discretization. In Table 4, for fixed  $\delta$  and  $L_{min}$ , we report on the error  $\|u - u_h\|_{L^2}$  and the computed convergence rate  $p_2$ , starting from  $\varepsilon = 0.1$  and progressively halving it. To minimize the interpolation error  $C_i h^{p_1}$  and the integration error  $E_i$ , so that the overall error is dominated by the  $\varepsilon$ -contribution, for each  $\varepsilon$ , during the tests the number of adaptive refinements  $L_{max}$  and of the mesh level  $ml$  have been increased with a brute force procedure until the values of the overall error did not change significantly

Table 2:  $h$ -Convergence test: errors  $\|u - u_h\|_{L^2}$  and computed order  $p$  as the mesh level  $ml$  increases for  $u = x^3 + y^3$ ,  $L_{min} = 1$ ,  $L_{max} = 3$ ,  $\delta = 0.2$ ,  $h_0 = 0.1$ ,  $h = h_0(1/2)^{ml-2}$ ,  $\varepsilon_0 = 0.0125$ ,  $\varepsilon = \varepsilon_0(2/3)^{ml-2}$ .

$ml$	QUAD		TRI		MIXED	
	bilinear	quadratic	linear	quadratic	linear	quadratic
2	4.363E-03 <b>1.996</b>	6.077E-05 <b>3.090</b>	4.373E-03 <b>1.999</b>	6.389E-05 <b>3.015</b>	2.386E-03 <b>2.028</b>	3.352E-05 <b>3.188</b>
3	1.094E-03 <b>1.998</b>	7.135E-06 <b>2.995</b>	1.094E-03 <b>1.999</b>	7.906E-06 <b>2.989</b>	5.848E-04 <b>2.015</b>	3.677E-06 <b>2.865</b>
4	2.738E-04 <b>2.000</b>	8.950E-07 <b>2.690</b>	2.737E-04 <b>1.999</b>	9.956E-07 <b>2.694</b>	1.447E-04 <b>2.006</b>	5.046E-07 <b>1.674</b>
5	6.845E-05 <b>2.000</b>	1.387E-07 <b>1.012</b>	6.845E-05 <b>2.000</b>	1.538E-07 <b>1.315</b>	3.602E-05 <b>2.003</b>	1.581E-07 <b>0.880</b>
6	1.711E-05	6.878E-08	1.711E-05	6.179E-08	8.983E-06	8.589E-08

Table 3:  $h$ -Convergence test: errors  $\|u - u_h\|_{L^2}$  and computed order  $p$  as the mesh level  $ml$  increases for  $u = x^4 + y^4$ ,  $L_{min} = 1$ ,  $L_{max} = 3$ ,  $\delta = 0.2$ ,  $h_0 = 0.1$ ,  $h = h_0(1/2)^{ml-2}$ ,  $\varepsilon_0 = 0.0125$ ,  $\varepsilon = \varepsilon_0(2/3)^{ml-2}$ .

$ml$	QUAD		TRI		MIXED	
	bilinear	quadratic	linear	quadratic	linear	quadratic
2	6.383E-03 <b>1.972</b>	9.544E-05 <b>2.892</b>	6.398E-03 <b>1.976</b>	1.027E-04 <b>2.914</b>	3.267E-03 <b>2.005</b>	5.561E-05 <b>2.769</b>
3	1.627E-03 <b>1.986</b>	1.285E-05 <b>2.161</b>	1.626E-03 <b>1.985</b>	1.362E-05 <b>2.240</b>	8.138E-04 <b>2.000</b>	8.155E-06 <b>1.677</b>
4	4.106E-04 <b>1.990</b>	2.872E-06 <b>1.374</b>	4.105E-04 <b>1.990</b>	2.883E-06 <b>1.373</b>	2.034E-04 <b>1.994</b>	2.550E-06 <b>1.214</b>
5	1.033E-04 <b>1.990</b>	1.108E-06 <b>1.178</b>	1.033E-04 <b>1.990</b>	1.113E-06 <b>1.176</b>	5.106E-05 <b>1.988</b>	1.099E-06 <b>1.159</b>
6	2.599E-05	4.895E-07	2.599E-05	4.923E-07	1.287E-05	4.920E-07

anymore. The error values reported in the table are those obtained only after this steady state was reached. The interpolation error (IE) in the table is reported as a reference and is obtained by numerically solving the local counterpart of the nonlocal Poisson problem at the finer mesh level, i.e. the one to which is associated the steady state. Also as a reference, we report the relative error (RE) between the interpolation error and the overall error

$$\text{RE} = \frac{\text{IE}}{\|u - u_h\|_{L^2(\Omega \cup \Gamma)}}.$$

The smaller the value of RE the more accurate the data, since the impact of the interpolation error on the overall error vanishes. The  $\varepsilon$ -convergence order is deliberately computed as

$$p_2 \approx \ln(E(\varepsilon)/E(\varepsilon/2))/\ln(2), \quad (44)$$

and is approximately  $p_2 \approx 2$  for all the tested mollifier thicknesses.

**Comparison with other algorithms** In Section 5.1 we introduced the maximum and minimum distance between elements in order to determine all elements intersecting the ball that identifies the support of the kernel function, for which integration is performed. However, in the literature, there are other techniques to determine whether an element should be considered during the assembly of the FE matrix. As an example, the paper by D'Elia et al.[22] proposes a technique for which only the elements whose barycenter lies inside the ball are considered for integration. This approach results in an approximation of the ball by a union of whole finite elements, and shows second order  $h$ -convergence for all FE spaces (linear, quadratic, etc.), as the rate is determined by the ball approximation. With the purpose of testing the performance of our method against current approaches, we conduct a comparison study, where we consider two different values of  $\varepsilon$  and compare our results with those obtained with a barycenter approach. Specifically, we use  $\varepsilon_0 = 0.0125$ , with  $\varepsilon = \varepsilon_0(2/3)^{ml-2}$  and  $\varepsilon_0 = 0.0250$ , with

Table 4:  $\varepsilon$ -Convergence test:  $\|u - u_h\|_{L^2}$  and computed order  $p_2$  as  $\varepsilon$  decreases for  $u = x^4 + y^4$ ,  $\delta = 0.2$ ,  $L_{min} = 1$ , and quadratic FE.

$\varepsilon$	<b>IE</b>	<b>TRI</b>	<b>RE</b>
0.1	1.602E-06	7.107E-04 <b>2.09</b>	2.25E-03
0.05	1.602E-06	1.671E-04 <b>1.90</b>	9.58E-03
0.025	1.602E-06	4.4716E-05 <b>1.91</b>	3.58E-02
0.0125	2.002E-07	1.189E-05 <b>1.95</b>	1.68E-02
0.00625	2.002E-07	3.073E-06 <b>1.92</b>	6.51E-02
0.00313	2.002E-07	8.117E-07	2.46E-01

Table 5: Comparison test: errors  $\|u - u_h\|_{L^2}$  and  $h$ -convergence rate  $p$  with a quadrilateral mesh and linear FE as the mesh refinement level  $ml$  increases for  $u = x^4 + y^4$ ,  $\delta = 0.2$ ,  $h_0 = 0.1$ ,  $h = h_0(1/2)^{ml-2}$ . For the adaptive algorithm: (Legendre  $3 \times 3$ )  $\times$  (Legendre  $3 \times 3$ ),  $L_{min} = 1$ ,  $L_{max} = 3$ . For the barycenter algorithm: (Lobatto  $3 \times 3$ )  $\times$  (Legendre  $3 \times 3$ )

$ml$	<b>IE</b>	<b>Adaptive</b>		<b>Barycenter</b>
	-	$\varepsilon = 0.0125 (2/3)^{ml-2}$	$\varepsilon = 0.025 (1/2)^{ml-2}$	
2	3.280E-03 <b>1.99</b>	3.281E-03 <b>2.02</b>	3.290E-03 <b>2.01</b>	5.428E-03 <b>1.95</b>
3	8.250E-04 <b>2.00</b>	8.092E-04 <b>1.99</b>	8.147E-04 <b>2.00</b>	1.401E-03 <b>1.82</b>
4	2.066E-04 <b>2.00</b>	2.034E-04 <b>1.99</b>	2.038E-04 <b>2.00</b>	3.974E-04 <b>2.00</b>
5	5.168E-05 <b>2.01</b>	5.118E-05 <b>1.99</b>	5.104E-05 <b>2.00</b>	9.909E-05 <b>1.69</b>
6	1.287E-05 <b>1.99</b>	1.287E-05 <b>1.98</b>	1.273E-05 <b>2.00</b>	3.073E-05 <b>1.67</b>
7	3.231E-06	3.270E-06	3.195E-06	9.645E-06

$\varepsilon = \varepsilon_0(1/2)^{ml-2}$  (note that the  $\varepsilon$  decrease differently). For the the adaptive quadrature rule presented in this paper we use a Legendre quadrature rule both for the internal and external integral, whereas for the barycenter method we use a hybrid Lobatto  $\times$  Legendre quadrature rule, Lobatto in the outer integral and Legendre in the inner one. In Table 5 we report the discretization errors for linear FE on a quadrilateral mesh as the mesh level  $ml$  increases. The  $h$ -convergence rate  $p$  is computed as in (42). We see that this rate is always optimal ( $p \approx 2$ ) regardless of the value of  $\varepsilon$ ; in other words, the mollifier and numerical quadrature contributions are negligible and the error is dominated by the FE interpolation contribution. On the other hand, the barycenter method shows bigger errors and less regular convergence order, due to geometric error introduced by the ball approximation. The computational times are all comparable since  $L_{max}$  has been taken equal to 1, and all quadrature rules have the same number of points. The interpolation error IE reported in the table has the same meaning as already discussed.

## 6.2 Three-dimensional tests

Three-dimensional simulations of nonlocal problems are incredibly challenging, especially in a variational setting, due to the prohibitively high computational effort. At the time of this study, the nonlocal literature still does not offer efficient, scalable algorithms for three-dimensional FE implementations of nonlocal solvers for kernels with bounded support. Efficient algorithms for fractional operators are proposed in [1], whereas implementations for compactly-supported, integrable kernels on structured grids can be found

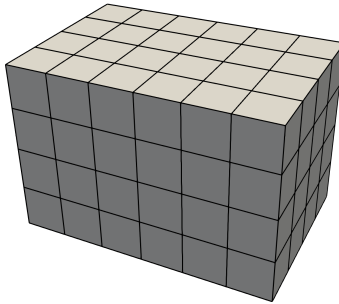


Figure 3: Hexahedron mesh used for the three-dimensional numerical simulations, with  $N_h = 175$  (linear FE discretization) and  $N_h = 605$  (quadratic FE discretization).

Table 6: Consistency in 3D:  $h = 0.1$ ,  $\delta = 0.2$ ,  $\varepsilon_0 = 0.0125$ ,  $u = x^2 + y^2 + z^2$ ,  $L_{min} = 1$ ,  $\varepsilon = \varepsilon_0 \left(\frac{3}{4}\right)^{L_{max}-2}$ , quadratic FE.

$\ u - u_h\ _{L^2}$	
$L_{max}$	HEX
2	6.863E-04
3	2.499E-05
4	3.241E-06
5	7.035E-08

in [53] and [52]. Here, not only do we introduce an efficient three-dimensional implementation, but we also propose a scalable, parallel implementation.

We proceed as in the two-dimensional case. In all our tests we consider the numerical domain  $\Omega = [-0.6, 0.6] \times [-0.4, 0.4] \times [-0.4, 0.4]$ , discretized with the regular hexahedron mesh reported in Figure 3.

We first consider a consistency test; for fixed values of  $\delta$ ,  $L_{min}$  and  $h$  we increase the refinement level  $L_{max}$ . For the same reasons explained in the previous section, we consider the analytic solution  $u = x^2 + y^2 + z^2$  for which the corresponding forcing term is given by  $f(\mathbf{x}) = -6$  for  $\mathbf{x} \in \Omega$ . Results for quadratic FE on the structured hexahedral mesh are reported in Table 6. As expected, the error decreases when the adaptive refinement level  $L_{max}$  is increased, illustrating the consistency of the adaptive algorithm in three dimensions.

Next, we test the  $h$ -convergence on the structured hexahedral mesh for both linear and quadratic FE. For the analytic solution  $u(\mathbf{x}) = x^3 + y^3 + z^3$  and fixed  $L_{min}$ ,  $L_{max}$ , and  $\delta$  we study the behavior of the error  $\|u - u_h\|_{L^2}$  as we halve  $h$ . Here, the corresponding source term is  $f(\mathbf{x}) = -\Delta u(\mathbf{x}) = -\mathcal{L}u = -6(x + y + z)$  for  $\mathbf{x} \in \Omega$ . In Table 7 (left), we report on the errors and the computed convergence rate  $p$ . We also consider the analytic solution  $u(\mathbf{x}) = x^4 + y^4 + z^4$  with the corresponding source term  $f(\mathbf{x}) = -12(x^2 + y^2 + z^2) - 6/7\delta^2$  for  $\mathbf{x} \in \Omega$ . For the same parameters as for the cubic polynomial, results of numerical experiments are reported in Table 7 (right). We observe an optimal convergence rate  $p \approx 2$  for linear FE discretizations for both the cubic and the quartic cases. Similarly to the two dimensional case, the convergence rate for the quadratic FE discretizations starts from  $p \approx 3$  and it deteriorates when  $ml$  grows. In general, the three-dimensional numerical results are consistent with the two-dimensional ones and the same considerations can be inferred.

### 6.3 Parallel implementation

The high computational effort necessary to perform three-dimensional nonlocal simulations requires a parallel implementation, even for relative small-sized problems. This is mostly due to the fact that, unlike what happens in the local settings, the bandwidth of a nonlocal matrix increases with mesh refinement, since the radius,  $\delta$ , of the nonlocal neighborhood remains fixed. In this section, we first highlight the need of a parallel implementation, we then propose a parallel algorithm, and finally illustrate its efficiency on two- and three-dimensional problems.

**Complexity of nonlocal simulations** For each refinement, i.e. every time the mesh size is halved, the average number of elements contained in the kernel's support increases of a factor  $2^N$ . Consequently,

Table 7:  $h$ -convergence: errors  $\|u - u_h\|_{L^2}$  and convergence rate  $p$  as the mesh level  $ml$  increases for  $u = x^3 + y^3 + z^3$  (left) and  $u = x^4 + y^4 + z^4$  (right),  $L_{min} = 1$ ,  $L_{max} = 2$ ,  $\delta = 0.2$ ,  $h_0 = 0.2$ ,  $h = h_0(1/2)^{ml-1}$ ,  $\varepsilon_0 = 0.01875$ ,  $\varepsilon = \varepsilon_0(2/3)^{ml-1}$ .

HEX			HEX		
$ml$	linear	quadratic	$ml$	linear	quadratic
1	2.220E-02 <b>1.988</b>	6.739E-04 <b>2.972</b>	1	3.299E-02 <b>1.964</b>	9.328E-04 <b>2.864</b>
2	5.593E-03 <b>1.998</b>	8.587E-05 <b>2.797</b>	2	8.452E-03 <b>1.985</b>	1.281E-04 <b>2.674</b>
3	1.400E-03 <b>1.999</b>	1.235E-05 <b>2.816</b>	3	2.134E-03 <b>1.992</b>	2.006E-05 <b>2.303</b>
4	3.501E-04	1.753E-06	4	5.361E-04	4.064E-06

the number of unknowns increases of the same factor and the number of nonzero entries in the matrix increases of  $2^{2N}$ , as opposed to local settings where the average increase at every mesh refinement is  $2^N$ . To better understand the impact of such increase let us consider the quadrilateral mesh used in the previous simulations for the quadratic solution, with a sparse matrix where the allocation for a non-zero entry is 12-bytes: 4 to specify the column location in the row (int) and 8 to store the value (double). At mesh level  $ml = 6$ , the number of unknowns is  $N_h = 148353$  and, for  $\delta = 0.2$ , the maximum number of entries in one row is 34749. The memory allocation for this mesh level requires approximately 80 GB of memory, while a corresponding local problem would require no more than 50 MB of memory.

Similarly, for each mesh refinement, the computational time to assemble the nonlocal matrix increases in average by the same factor  $2^{2N}$ , since the number of elements increases of  $2^N$  and the average number of elements contained inside the kernel's support increases by  $2^N$ . For a local problem the assembly time increases only of a factor  $2^N$ . These differences in memory allocation and CPU time indicate that a parallel implementation of the nonlocal assembly is vital to make nonlocal models a preferred and viable modeling option.

**Details on the implementation** We begin our description by stressing the fact that, even in a local context, a parallel implementation of a FE algorithm is nontrivial. In what follows, we assume that the reader is familiar with the FE method and relatively accustomed to its parallel implementation [5]; thus, we proceed by highlighting the main challenges that arise in nonlocal implementations.

Our parallel algorithm has been implemented in FEMuS [4] and is publicly available on GitHub. FEMuS is an in-house FE C++ library that interfaces with PETSc [6], which provides the linear algebra library for the parallel solver. The parallelization of the nonlocal assembly has been entirely developed within FEMuS.

As it is common in parallel FE settings, the mesh elements are partitioned among the processes  $N_p$ ; FEMuS uses the METIS/PARAMETIS [32] library for partitioning unstructured meshes. For each process  $I$ , we let  $\Omega_I$  be the domain composed of the elements owned by  $I$  that overlap with  $\Omega$  and  $\Pi_I$  be the domain composed of the elements owned by  $I$  that overlap with  $\Gamma$ . Although highly desirable, each sub-domain  $\Omega_I \cup \Pi_i$  does not need to be simply connected. Similar to the definition of  $\Gamma$ , we define the interaction domain  $\Gamma_I$  of  $\Omega_I$  as

$$\Gamma_I = \{\mathbf{y} \in (\Omega \cup \Gamma) \setminus \Omega_I : |\mathbf{x} - \mathbf{y}| \leq \delta + \varepsilon \text{ for some } \mathbf{x} \in \Omega_I \cup \Pi_I\}. \quad (45)$$

While in the local case two processes  $I$  and  $J$  have to exchange information only between elements on a shared boundary, i.e. on  $\partial\Omega_I \cap \partial\Omega_J$ , in the nonlocal case the two processes need to exchange information whenever an element of  $I$  intersects the interaction domain  $\Gamma_J$  or vice-versa. We denote by  $\Gamma_{JI}$  the region made up by all the elements owned by process  $J$  that intersect with the interaction domain  $\Gamma_I$ , for  $I, J = 1, \dots, N_p$ . Set  $\tilde{\Gamma}_I = \cup_{J \in N_p} \Gamma_{JI}$ . The following relations hold

$$\begin{aligned} \Gamma_{JI} \cap \Gamma_{KI} &= \emptyset \text{ for } J \neq K, \\ \Gamma_I &\subseteq \tilde{\Gamma}_I, \\ \Gamma_{II} &= \Pi_I, \\ \Gamma &= \cup_{I \in N_p} \Gamma_{II}, \\ \Gamma_{II} \cap \Gamma_{JJ} &= \emptyset \text{ for } I \neq J. \end{aligned}$$

The following expression clarifies what operations can be performed within one process and which ones require exchange of information among processes. We consider a general integral, whose numerical



computation is ubiquitous in Algorithm 1. For any function  $w(\mathbf{x}, \mathbf{y})$ , any double integral such as those defined in the first part of the paper can be rewritten as

$$\begin{aligned}
& \iint_{(\Omega \cup \Gamma)^2} \gamma_\epsilon(\mathbf{x}, \mathbf{y}) w(\mathbf{x}, \mathbf{y}) d\mathbf{y} d\mathbf{x} \\
&= \sum_{I=1}^{N_p} \int_{\Omega \cup \Gamma} \int_{\Omega_I \cup \Gamma_{II}} \gamma_\epsilon(\mathbf{x}, \mathbf{y}) w(\mathbf{x}, \mathbf{y}) d\mathbf{y} d\mathbf{x} \\
&= \sum_{I=1}^{N_p} \int_{\Omega_I \cup \Gamma_I} \int_{\Omega_I \cup \Gamma_{II}} \gamma_\epsilon(\mathbf{x}, \mathbf{y}) w(\mathbf{x}, \mathbf{y}) d\mathbf{y} d\mathbf{x} \\
&= \sum_{I=1}^{N_p} \int_{\Omega_I \cup \tilde{\Gamma}_I} \int_{\Omega_I \cup \Gamma_{II}} \gamma_\epsilon(\mathbf{x}, \mathbf{y}) w(\mathbf{x}, \mathbf{y}) d\mathbf{y} d\mathbf{x} \\
&= \sum_{I=1}^{N_p} \int_{\Omega_I \cup (\cup_{J \in N_p} \Gamma_{JI})} \int_{\Omega_I \cup \Gamma_{II}} \gamma_\epsilon(\mathbf{x}, \mathbf{y}) w(\mathbf{x}, \mathbf{y}) d\mathbf{y} d\mathbf{x} \\
&= \sum_{I=1}^{N_p} \left( \iint_{(\Omega_I \cup \Gamma_{II})^2} \gamma_\epsilon(\mathbf{x}, \mathbf{y}) w(\mathbf{x}, \mathbf{y}) d\mathbf{y} d\mathbf{x} + \sum_{\substack{J=1 \\ J \neq I}}^{N_p} \int_{\Gamma_{JI}} \int_{\Omega_I \cup \Gamma_{II}} \gamma_\epsilon(\mathbf{x}, \mathbf{y}) w(\mathbf{x}, \mathbf{y}) d\mathbf{y} d\mathbf{x} \right) \\
&= \sum_{I=1}^{N_p} \left( \iint_{(\Omega_I \cup \Gamma_{II})^2} \gamma_\epsilon(\mathbf{x}, \mathbf{y}) w(\mathbf{x}, \mathbf{y}) d\mathbf{y} d\mathbf{x} + \sum_{\substack{J=1 \\ J \neq I}}^{N_p} \int_{\Gamma_{JI}} \int_{(\Omega_I \cup \Gamma_{II}) \cap \tilde{\Gamma}_J} \gamma_\epsilon(\mathbf{x}, \mathbf{y}) w(\mathbf{x}, \mathbf{y}) d\mathbf{y} d\mathbf{x} \right) \\
&= \sum_{I=1}^{N_p} \left( \iint_{(\Omega_I \cup \Gamma_{II})^2} \gamma_\epsilon(\mathbf{x}, \mathbf{y}) w(\mathbf{x}, \mathbf{y}) d\mathbf{y} d\mathbf{x} + \sum_{\substack{J=1 \\ J \neq I}}^{N_p} \int_{\Gamma_{JI}} \int_{\Gamma_{IJ}} \gamma_\epsilon(\mathbf{x}, \mathbf{y}) w(\mathbf{x}, \mathbf{y}) d\mathbf{y} d\mathbf{x} \right). \tag{46}
\end{aligned}$$

A few remarks are in order. In the last equality the first double integral relies on information fully available on process  $I$ . In contrast, the outer integrals of the second term are defined on sub-domains  $\Gamma_{JI}$ , which belong to processes different from  $I$ . Thus, for process  $I$ , this information has to be made available through parallel implementation. Namely, before integration, each process  $J$  sends to  $I$  the needed information stored in the elements that make up  $\Gamma_{JI}$  through the MPI send/receive protocol [29]. The inner integral is on the sub-region  $\Gamma_{IJ}$  owned by process  $I$ . In the definition of  $A_{ij}^{21}$  and  $A_{ij}^{22}$ , the inner integral identifies the  $i$ -th row of the matrix through the test function  $\varphi_i(\mathbf{y})$ . Hence, the degree of freedom of that row is owned by process  $I$ . We allocate the memory to store the entries of each row of the sparse parallel matrix on the process that owns the row itself; this results in an optimal parallel assembly since it minimizes (almost removes) the communication time.

**Remark 2** *As already pointed out in Section 5.1, identifying if a given element intersect a given region can be challenging and computationally expensive. As described before, we rely on a simple and fast conservative test to identify if an element  $\mathcal{E}_j$ , owned by process  $J$  belongs to  $\Gamma_{JI}$ . Namely, we use formula (37) to approximate the minimum distance between the bounding box enveloping  $\mathcal{E}_j$  and the bounding box enveloping all the elements owned by processor  $I$ . If the approximate distance is less than  $\delta + \epsilon$ , then  $\mathcal{E}_j$  is included into  $\Gamma_{JI}$ .*

**Performance tests** We first consider two-dimensional problems with both linear and quadratic FE discretizations with 480641 and 1440513 degrees of freedom, respectively. We consider a quadrilateral mesh with  $ml = 7$  (for which  $h = 1.5625\text{E-}03$ ),  $\epsilon = h/2$ ,  $\delta = 0.05$ ,  $L_{max} = 3$ ,  $L_{min} = 1$ . Since the high computational costs are mainly due to the assembly procedure, we report separately the CPU times required by the assembly routine ( $t_a$ ) and the total CPU time ( $t_t$ ), which also includes the solver time. Computational times, as the number of processors  $N_p$  grows, are reported in Table 8. We also report the time ratios  $\text{TR}_a(N_p) = t_a(N_p/2)/t_a(N_p)$  and  $\text{TR}_t(N_p) = t_t(N_p/2)/t_t(N_p)$ . All cases feature large time ratios, illustrating the good scaling properties of the parallel implementation for both linear and quadratic FE discretizations.

We also test the scaling properties of the parallel algorithm with three-dimensional numerical simulations. Similarly to the two-dimensional case, we consider a hexahedral mesh with 615489 degrees of

Table 8: Assembly time  $t_a$  and total time  $t_t$  of simulations with 480641 dofs, linear FEM, and 1440513 dofs, quadratic FEM,  $h = 1.5625\text{E-}03$ ,  $\varepsilon = h/2$ ,  $\delta = 0.05$ ,  $L_{max} = 3$ ,  $L_{min} = 1$ .

$N_p$	Linear		Quadratic	
	$t_a$ [s]	$t_t$ [s]	$t_a$ [s]	$t_t$ [s]
36	4268.57	4470.87	1795.86	2168.10
	<b>1.89</b>	<b>1.90</b>	<b>1.77</b>	<b>1.68</b>
72	2251.59	2346.46	1013.76	1290.14
	<b>1.92</b>	<b>1.94</b>	<b>1.88</b>	<b>1.94</b>
144	1166.77	1207.84	538.12	663.53
	<b>1.72</b>	<b>1.73</b>	<b>1.64</b>	<b>1.70</b>
288	675.67	694.44	327.75	388.88
	<b>1.85</b>	<b>1.85</b>	<b>1.65</b>	<b>1.72</b>
576	364.65	373.77	197.83	225.32

Table 9: Assembly time  $t_a$ , total time  $t_t$  and time ratios of simulations with 615489 dofs, quadratic FEM,  $h = 0.025$ ,  $\varepsilon = h/2$ ,  $\delta = 0.1$ ,  $L_{max} = 2$ ,  $L_{min} = 1$ .

$N_p$	$t_a$ [s]	$t_t$ [s]
36	17598.5	17727.83
	<b>1.92</b>	<b>1.92</b>
72	9155.14	9223.08
	<b>2.00</b>	<b>2.00</b>
144	4556.1	4591.51
	<b>1.99</b>	<b>1.97</b>
288	2286.17	2314.36

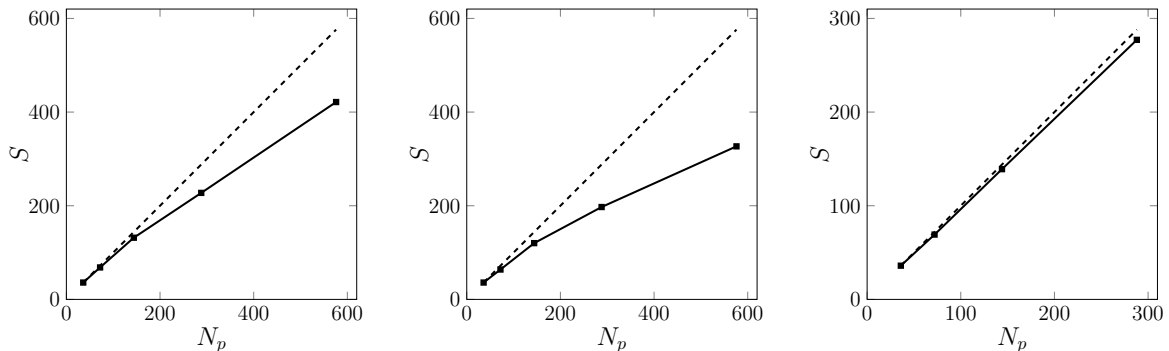


Figure 4: Speedup as a function of the number of processors for two-dimensional linear (left) and quadratic FE (center), and three-dimensional quadratic FE (right).

freedom and a quadratic FE discretization. We also set  $h = 0.025$ ,  $\varepsilon = h/2$ ,  $\delta = 0.1$ ,  $L_{max} = 2$ ,  $L_{min} = 1$ . In Table 9 we report the assembly time  $t_a$ , the total time  $t_t$  and the time ratios of the numerical simulation for increasing number of processes. As in the two-dimensional case, the parallel simulations show high time ratios, indicating good scaling properties of the algorithm.

In Figure 4 we show the assembly speedup  $S$  values referred to  $N_p = 36$ , defined as  $S = t_a(36)/t_a(N_p)$  for two-dimensional linear (left), quadratic (center) and three-dimensional quadratic (right) simulations. We also report the linear speedup (dashed line). On the basis of the presented results, the code shows excellent scalability properties especially in 3D. Thus, it proves to be suitable for large scale nonlocal simulations.

## 7 Conclusion

We introduced an efficient, flexible, and scalable algorithm for FE discretizations of nonlocal diffusion problems characterized by compactly supported kernels. The novelty of our work is three fold. First, we circumvent the numerical difficulties arising from the integration of discontinuous kernels by multiplying the integrand function by a mollifier. This allows us to avoid the tedious and costly process of identifying ball-element intersections, hence avoiding integration over partial elements and/or curved elements. These tasks, even though manageable in two-dimensional settings, become nontrivial in three dimensions. Second, we introduce an adaptive quadrature rule that allows us accurately resolve the high gradients featured by the integrand function without compromising the computational efficiency. Third, we propose a parallel implementation of the mollified, adaptive algorithm that shows excellent scalability properties especially in three dimensions, where the cost of numerical integration dominates. Our numerical results illustrate the theoretical findings and show that, in two dimensions, our algorithm is competitive with other efficient approximations of FE implementations. In three dimensions, this is the first efficient and scalable parallel implementation that has no constraints on the type of mesh or FE spaces.

As such, this work contributes to making variational discretizations of nonlocal models a viable option, even for large scale problems. It also represents an effort towards increasing the usability of nonlocal equations, for which the high computational costs often hinders their popularity in engineering contexts, despite their undeniable improved accuracy.

## Supporting information

This work was supported by the National Science Foundation (NSF) Division of Mathematical Sciences (DMS) program, project 1912902, by Sandia National Laboratories (SNL) Laboratory-directed Research and Development (LDRD) program, project 218318 and by the U.S. Department of Energy, Office of Advanced Scientific Computing Research under the Collaboratory on Mathematics and Physics-Informed Learning Machines for Multiscale and Multiphysics Problems (PhILMs) project. Sandia National Laboratories is a multimission laboratory managed and operated by National Technology and Engineering Solutions of Sandia, LLC., a wholly owned subsidiary of Honeywell International, Inc., for the U.S. Department of Energy's National Nuclear Security Administration contract number DE-NA0003525. This paper, SAND2021-0672, describes objective technical results and analysis. Any subjective views or opinions that might be expressed in the paper do not necessarily represent the views of the U.S. Department of Energy or the United States Government.

## References

- [1] M. Ainsworth and C. Glusa. Aspects of an adaptive finite element method for the fractional Laplacian: A priori and a posteriori error estimates, efficient implementation and multigrid solver. *Computer Methods in Applied Mechanics and Engineering*, 327:4–35, 2017.
- [2] M. Ainsworth and C. Glusa. Towards an efficient finite element method for the integral fractional Laplacian on polygonal domains. In *Contemporary Computational Mathematics-A Celebration of the 80th Birthday of Ian Sloan*, pages 17–57. Springer, 2018.
- [3] B. Alali and M. Gunzburger. Peridynamics and material interfaces. *Journal of Elasticity*, 120(2):225–248, 2015.
- [4] Eugenio Aulisa, Simone Bna, and Giorgio Bornia. FEMuS. <https://github.com/eaulisa/MyFEMuS.git>, 2014.
- [5] Ivo Babuška and Howard C Elman. Some aspects of parallel implementation of the finite-element method on message passing architectures. In *Advances in Parallel Computing*, volume 1, pages 157–187. Elsevier, 1990.
- [6] Satish Balay, Shrirang Abhyankar, Mark Adams, Jed Brown, Peter Brune, Kris Buschelman, Lisandro Dalcin, Alp Dener, Victor Eijkhout, W Gropp, et al. *PETSc users manual*. Argonne National Laboratory, 2019.
- [7] D. Benson, S. Wheatcraft, and M. Meerschaert. Application of a fractional advection-dispersion equation. *Water Resources Research*, 36(6):1403–1412, 2000.
- [8] D.A. Benson, R. Schumer, M.M. Meerschaert, and S.W. Wheatcraft. Fractional dispersion, Lévy motion, and the MADE tracer tests. *Transport in Porous Media*, 42:211–240, 2001.

- [9] A. Buades, B. Coll, and J. Morel. Image denoising methods. A new nonlocal principle. *SIAM Review*, 52:113–147, 2010.
- [10] N. Burch, M. D’Elia, and R. Lehoucq. The exit-time problem for a Markov jump process. *The European Physical Journal Special Topics*, 223:3257–3271, 2014.
- [11] Olena Burkovska, Christian Glusa, and Marta D’Elia. An optimization-based approach to parameter learning for fractional type nonlocal models. Preprint arXiv:2010.03666, 2020.
- [12] G. Capodaglio, M. D’Elia, P. Bochev, and M. Gunzburger. An energy-based coupling approach to nonlocal interface problems. *Computers and Fluids*, 2020.
- [13] G. Capodaglio, M. D’Elia, M. Gunzburger, P. Bochev, M. Klar, and C. Vollmann. A general framework for substructuring-based domain decomposition methods for models having nonlocal interactions. arXiv:2008.11780, 2020.
- [14] Youping Chen, James Lee, and Azim Eskandarian. *Meshless methods in solid mechanics*. Springer Science & Business Media, 2006.
- [15] C. Cortazar, M. Elgueta, J. Rossi, and N. Wolanski. How to approximate the heat equation with Neumann boundary conditions by nonlocal diffusion problems. *Archive for Rational Mechanics and Analysis*, 187:137–156, 2008.
- [16] M. D’Elia, J.-C. De los Reyes, and A. Miniguano-Trujillo. Bilevel parameter optimization for nonlocal image denoising models. arXiv:1912.02347, 2019.
- [17] M. D’Elia, Q. Du, C. Glusa, X. Tian, and Z. Zhou. Numerical methods for nonlocal and fractional models. *ACTA Numerica*, 29, 2020.
- [18] M. D’Elia, Q. Du, M. Gunzburger, and R. Lehoucq. Nonlocal convection-diffusion problems on bounded domains and finite-range jump processes. *Computational Methods in Applied Mathematics*, 29:71–103, 2017.
- [19] M. D’Elia, M. Gulian, H. Olson, and G. E. Karniadakis. A unified theory of fractional, nonlocal, and weighted nonlocal vector calculus. arXiv:2005.07686, 2020.
- [20] M. D’Elia and M. Gunzburger. Optimal distributed control of nonlocal steady diffusion problems. *SIAM Journal on Control and Optimization*, 55:667–696, 2014.
- [21] M. D’Elia and M. Gunzburger. Identification of the diffusion parameter in nonlocal steady diffusion problems. *Applied Mathematics and Optimization*, 73:227–249, 2016.
- [22] M. D’Elia, M. Gunzburger, and C. Vollmann. A cookbook for finite element methods for nonlocal problems, including quadrature rule choices and the use of approximate neighborhoods. arXiv:2005.10775, 2020.
- [23] M. D’Elia, X. Tian, and Y. Yu. A physically-consistent, flexible and efficient strategy to convert local boundary conditions into nonlocal volume constraints. *SIAM Journal of Scientific Computing*, 42(4):A1935–A1949, 2020.
- [24] Z.-Q. Deng, V.P. Singh, and L. Bengtsson. Numerical solution of fractional advection-dispersion equation. *Journal of Hydraulic Engineering*, 130(5), 2004.
- [25] Q. Du, M. Gunzburger, R. Lehoucq, and K. Zhou. Analysis and approximation of nonlocal diffusion problems with volume constraints. *SIAM Review*, 54(4):667–696, 2012.
- [26] Qiang Du, Max Gunzburger, R. Lehoucq, and Kun Zhou. A nonlocal vector calculus, nonlocal volume-constrained problems, and nonlocal balance laws. *Mathematical Models and Methods in Applied Sciences*, 23:493–540, 2013.
- [27] Qiang Du, Max Gunzburger, Richard Lehoucq, and Kun Zhou. Analysis and approximation of nonlocal diffusion problems with volume constraints. *SIAM review*, 54:667–696, 2012.
- [28] G. Gilboa and S. Osher. Nonlocal linear image regularization and supervised segmentation. *Multiscale Model. Simul.*, 6:595–630, 2007.
- [29] William Gropp, William D Gropp, Ewing Lusk, Anthony Skjellum, and Argonne Distinguished Fellow Emeritus Ewing Lusk. *Using MPI: portable parallel programming with the message-passing interface*, volume 1. MIT press, 1999.

- [30] M. Gulian, M. Raissi, P. Perdikaris, and G. E. Karniadakis. Machine learning of space-fractional differential equations. *SIAM Journal on Scientific Computing*, 41(4):A2485–A2509, 2019.
- [31] Y. D. Ha and F. Bobaru. Characteristics of dynamic brittle fracture captured with peridynamics. *Engineering Fracture Mechanics*, 78(6):1156–1168, 2011.
- [32] George Karypis, Kirk Schloegel, and Vipin Kumar. *Parmetis: Parallel graph partitioning and sparse matrix ordering library*. University of Minnesota, 1997.
- [33] P. C. Di Leoni, T. A. Zaki, G. Karniadakis, and C. Meneveau. Two-point stress-strain rate correlation structure and non-local eddy viscosity in turbulent flows. Submitted to *Journal of Fluid Mechanics*, 2020.
- [34] D. Littlewood. Simulation of dynamic fracture using peridynamics, finite element modeling, and contact. Proceedings of the ASME 2010 International Mechanical Engineering Congress and Exposition, Vancouver, British Columbia, Canada, 2010.
- [35] Y. Lou, X. Zhang, S. Osher, and A. Bertozzi. Image recovery via nonlocal operators. *Journal of Scientific Computing*, 42:185–197, 2010.
- [36] R. W. Macek and S. A. Silling. Peridynamics via finite element analysis. *Finite Elements in Analysis and Design*, 43(15):1169–1178, 2007.
- [37] M. Meerschaert and A. Sikorskii. *Stochastic models for fractional calculus*. Studies in mathematics, Gruyter, 2012.
- [38] Tadele Mengesha and Qiang Du. Analysis of a scalar nonlocal peridynamic model with a sign changing kernel. *Discrete and Continuous Dynamical Systems - B*, 18(5):1415–1437, 2013.
- [39] R. Metzler and J. Klafter. The random walk’s guide to anomalous diffusion: a fractional dynamics approach. *Physics Reports*, 339:1–77, 2000.
- [40] R. Metzler and J. Klafter. The restaurant at the end of the random walk: recent developments in the description of anomalous transport by fractional dynamics. *Journal Physics A*, 37:161–208, 2004.
- [41] SE Mousavi, JE Pask, and N Sukumar. Efficient adaptive integration of functions with sharp gradients and cusps in n-dimensional parallelepipeds. *International journal for numerical methods in engineering*, 91(4):343–357, 2012.
- [42] G. Pang, M. D’Elia, M. Parks, and G. E. Karniadakis. nPINNs: nonlocal Physics-Informed Neural Networks for a parametrized nonlocal universal Laplacian operator. Algorithms and Applications. *Journal of Computational Physics*, 2020. To appear.
- [43] G. Pang, L. Lu, and G. E. Karniadakis. fPINNs: Fractional physics-informed neural networks. *SIAM Journal on Scientific Computing*, 41:A2603–A2626, 2019.
- [44] G. Pang, P. Perdikaris, W. Cai, and G. E. Karniadakis. Discovering variable fractional orders of advection–dispersion equations from field data using multi-fidelity Bayesian optimization. *Journal of Computational Physics*, 348:694 – 714, 2017.
- [45] M. Parks, D. Littlewood, J. Mitchell, and S. Silling. Peridigm Users Guide. Technical Report SAND2012-7800, Sandia National Laboratories, NM, USA, 2012.
- [46] M. Parks, P. Seleson, S. Plimpton, R. Lehoucq, and S. Silling. Peridynamics with LAMMPS:A User Guide. Technical Report SAND2010-5549, Sandia National Laboratories, NM, USA, 2010.
- [47] M. Pasetto. *Enhanced Meshfree Methods for Numerical Solution of Local and Nonlocal Theories of Solid Mechanics*. PhD thesis, University of California, San Diego, CA, 2019.
- [48] R. Schumer, D. Benson, M. Meerschaert, and B. Baeumer. Multiscaling fractional advection-dispersion equations and their solutions. *Water Resources Research*, 39(1):1022–1032, 2003.
- [49] R. Schumer, D. Benson, M. Meerschaert, and S. Wheatcraft. Eulerian derivation of the fractional advection-dispersion equation. *Journal of Contaminant Hydrology*, 48:69–88, 2001.
- [50] S. A Silling and E. Askari. A meshfree method based on the peridynamic model of solid mechanics. *Computers & structures*, 83(17-18):1526–1535, 2005.

- [51] S.A. Silling. Reformulation of elasticity theory for discontinuities and long-range forces. *Journal of the Mechanics and Physics of Solids*, 48:175–209, 2000.
- [52] C. Vollmann and V. Schulz. Exploiting multilevel toeplitz structures in high dimensional nonlocal diffusion. *Computing and Visualization in Science*, 20:29–46, 2019.
- [53] H. Wang and H. Tian. A fast and faithful collocation method with efficient matrix assembly for a two-dimensional nonlocal diffusion model. *Computer Methods in Applied Mechanics and Engineering*, 273:19 – 36, 2014.
- [54] H. Wang, K. Wang, and T. Sircar. A direct  $\mathcal{O}(N \log^2 N)$  finite difference method for fractional diffusion equations. *Journal of Computational Physics*, 229(21):8095–8104, 2010.
- [55] Xiao Xu, Marta D’Elia, and John Foster. A machine-learning framework for peridynamic material models with physical constraints. Preprint arXiv:2101.01095, 2021.
- [56] H. You, Y. Yu, S. Silling, and M. D’Elia. Data-driven learning of nonlocal models: from high-fidelity simulations to constitutive laws. Preprint arXiv:2012.04157, 2020.
- [57] H. You, Y. Yu, N. Trask, M. Gulian, and M. D’Elia. Data-driven learning of robust nonlocal physics from high-fidelity synthetic data. arXiv:2005.10076, 2020.